Implication of a galaxy-scale negative feedback by one of the most powerful multi-phase outflows in a hyper-luminous infrared galaxy at the intermediate redshift

XIAOYANG CHEN ^[D], ¹ MASAYUKI AKIYAMA ^[D], ² KOHEI ICHIKAWA ^[D], ³ YOSHIKI TOBA ^[D], ^{1,4,5} TOSHIHIRO KAWAGUCHI ^[D], ⁶ TAKUMA IZUMI ^[D], ⁷ TOSHIKI SAITO ^[D], ⁸ DAISUKE IONO ^[D], ⁷ MASATOSHI IMANISHI ^[D], ⁷ KIANHONG LEE ^[D], ^{2,7} HIROSHI NAGAI ^[D], ⁷ HIROFUMI NODA ^[D], ² ABDURRO'UF ^[D], ⁹ MITSURU KOKUBO ^[D], ⁷ AND NAOKI MATSUMOTO ^[D]

National Astronomical Observatory of Japan, 2-21-1 Osawa, Mitaka, Tokyo 181-8588, Japan
 Astronomical Institute, Tohoku University, 6-3 Aramaki, Aoba-ku, Sendai, Miyagi 980-8578, Japan
 Faculty of Science and Engineering, Waseda University, 1-6-1 Nishi-Waseda, Shinjuku-ku Tokyo 169-8050 Japan
 Academia Sinica Institute of Astronomy and Astrophysics, 11F of Astronomy-Mathematics Building, AS/NTU, No.1, Section 4, Roosevelt Road, Taipei 10617, Taiwan

⁵Research Center for Space and Cosmic Evolution, Ehime University, 2-5 Bunkyo-cho, Matsuyama, Ehime 790-8577, Japan
⁶Department of Economics, Management and Information Science, Onomichi City University, Hisayamada 1600-2, Onomichi, Hiroshima 722-8506, Japan

⁷ National Astronomical Observatory of Japan, 2-21-1, Osawa, Mitaka, Tokyo 181-8588, Japan
⁸ Department of Global Interdisciplinary Science and Innovation, Shizuoka University, 836 Ohya, Suruga-ku, Shizuoka-Shi, 422-8529, Japan

(Received August 19, 2024; Revised October 28, 2024; Accepted November 14, 2024)

Submitted to ApJ

ABSTRACT

Powerful, galactic outflows driven by Active Galactic Nuclei (AGNs) are commonly considered as a main mechanism to regulate star formation in massive galaxies. Ultra- and hyper-luminous IR galaxies (U/HyLIRGs) are thought to represent a transition phase of galaxies from a rapidly growing period to a quiescent status as gas swept out by outflows, providing a laboratory to investigate outflows and their feedback effects on the hosts. In this paper we report recent Gemini and ALMA observations of a HyLIRG, J1126 at z=0.46842, which has been identified with a puzzling co-existence of a fast ionized outflow (> 2000 km s⁻¹) and an intense starburst (star formation rate of 800 M_{\odot} yr⁻¹). The Gemini observation shows the fast ionized outflow is extended to several kpc with a mass-loss rate of 180 M_{\odot} yr⁻¹. A massive molecular outflow with a high mass-loss rate (2500 M_{\odot} yr⁻¹) is revealed by ALMA. The multi-phase outflows show large factors of momentum boost and loading of kinetic power, indicating a driving by thermal pressure of a nuclear hot wind and/or radiation pressure of a highly obscured AGN. In addition to ejection of kinetic energy, it is also found that the powerful outflow can induce an ionizing shock in the galaxy disk and enhance the excitation and dissociation of molecular gas. The powerful outflow probably results in an instantaneous negative feedback and shows potential to regulate the host growth in a long term.

 $\begin{tabular}{ll} Keywords: Active galactic nuclei (16) & --- Ultraluminous infrared galaxies (1735) & --- Galaxy winds (626) & --- Galaxy quenching (2040) \end{tabular}$

1. INTRODUCTION

It is widely accepted that the supermassive black holes (SMBHs) in the center of galaxies can affect the evolu-

Corresponding author: Xiaoyang Chen xiaoyang.chen@nao.ac.jp

tion of their host galaxies. Such association is supported by observational evidences, e.g., the relation between SMBH masses and properties of host stellar spheroids (masses and velocity dispersions; e.g., Ferrarese & Merritt 2000; Gebhardt et al. 2000; King 2005; Kormendy & Ho 2013), and the low gas cooling rate in massive galaxies in the center of clusters (e.g., Ciotti & Ostriker 1997; Peterson et al. 2003). The feedback by SMBHs

⁹ Department of Physics and Astronomy, Johns Hopkins University, 3400 N. Charles Street, Baltimore, MD 21218, US

is also required in simulations to explain the reduced star formation efficiency in massive galaxies as well as the bi-modal distribution of local galaxies in the stellar mass and star formation rate (SFR) diagram (e.g., Benson et al. 2003; Bower et al. 2006; Schaye et al. 2015; Khandai et al. 2015; Nelson et al. 2018). Powerful, galactic scale outflows are considered as a main feedback mechanism of SMBHs (e.g., Fabian 2012; King & Pounds 2015; Tombesi et al. 2015), which can either quench the star formation in the hosts via expelling out or heating the cold fueling gas (i.e., a negative feedback; e.g., Ellison et al. 2021; Saito et al. 2022a; Lammers et al. 2023), or promote the star formation by compressing the ambient gas (i.e., a positive feedback; e.g., Cresci et al. 2015; Maiolino et al. 2017; Shin et al. 2019). Those outflows are observed in multiple gas phases, i.e., from hot/warm ionized gas (e.g., Liu et al. 2013; Harrison et al. 2014; Zakamska et al. 2016; Toba et al. 2017a; Chen et al. 2019) to cold neutral atomic (e.g., Perna et al. 2020; Avery et al. 2022) and molecular gas (e.g., Sturm et al. 2011; Veilleux et al. 2013; Cicone et al. 2014). Although the contribution of an intense starburst to launch a powerful outflow is argued by several recent works (e.g., Geach et al. 2014; Rupke et al. 2019), it is usually considered that the outflows, especially those with a high velocity, are driven by SMBHs in a fast accretion mode, which are observed as Active Galactic Nuclei (AGNs; e.g., Cicone et al. 2014; Zakamska et al. 2016; Fiore et al. 2017).

Ultra- and hyper-luminous IR galaxies (ULIRGs, $L_{\rm IR} > 10^{12} L_{\odot}$; HyLIRGs, $L_{\rm IR} > 10^{13} L_{\odot}$) are thought to represent a transiting population of galaxies from a merger-induced, rapidly growing phase of SMBHs and stellar spheroids, to a quiescent status as the fueling gas swept out by powerful outflows (e.g., Hopkins et al. 2008; Sturm et al. 2011; Veilleux et al. 2013; Toba et al. 2022). The ubiquitousness of powerful outflows in U/HyLIRGs makes them laboratories to investigate the properties of outflows (e.g., velocity, extent, mass-loss rate) and their feedback effects on the hosts. Chen et al. (2020b) reported a sample of ~ 200 U/HyLIRGs at the intermediate redshifts (0.1 < z < 1.0) selected from the AKARI far-IR all-sky survey, which are cross-matched with SDSS (optical) and WISE (near- and mid-IR) photometric catalogs and spectroscopically identified with SDSS and Subaru/FOCAS observations. It is found that fast ionized outflows (e.g., $v_{10} > 1500 \text{ km s}^{-1}$, where v_{10} is the 10th percentile velocity of [OIII] line) and intense starbursts with IR-based SFR over 300 M_{\odot} yr⁻¹ co-exist in a few of U/HyLIRGs in the sample. The co-existence of fast outflows and intense starbursts suggest a possibility of an apparently "failed" feedback, i.e., the star formation activities have not been profoundly suppressed by the outflow. The puzzling results can be likely explained by a compact distribution of the outflow, i.e., only a limited volume of the star-forming regions can be affected by the outflow; or the different timescales of the outflow (several Myr; e.g., Harrison & Ramos Almeida

2024) and the IR-based SFR estimator (several tens to 100 Myr; e.g., Murphy et al. 2011), i.e., a possible instantaneous feedback cannot be reflected by the SFR in a long-term. It is also possible that the fast outflow only occurs in the ionized gas phase while the molecular gas clouds in which stars form are not effectively accelerated/dispersed (e.g., Toba et al. 2017b). A "delayed" feedback scenario may also provide an alternative explanation for the apparent non-quenching of star formation (e.g., Woo et al. 2017).

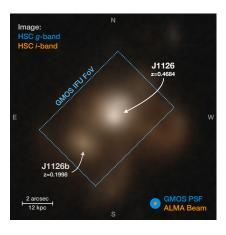
In order to shed light on the mechanisms behind the co-existence of fast ionized outflow and intense starbursts, we conducted follow-up observations for the U/HyLIRG sample with multi-wavelength telescopes. In this paper we report the recent observations with Gemini-N telescope and the Atacama Large Millimeter/submillimeter Array (ALMA) for one HyLIRG in the sample, AKARI-FIS-V2 J1126579+163917 (hereafter J1126; Figure 1) at z = 0.4684. J1126 has a total IR (1–1000 μ m) luminosity of $1.2 \times 10^{13} L_{\odot}$ and harbors a Type-2 AGN identified with optical emission lines and mid-IR radiation (Chen et al. 2020b). J1126 possesses one of the fastest ionized outflow $(v_{10} > 2000 \text{ km s}^{-1})$ and the most vigorous starburst (SFR $\sim 800~M_{\odot}~\rm{yr}^{-1}$) among U/HyLIRGs and AGNs at z < 1 (e.g., Arribas et al. 2014; Liu et al. 2013; Harrison et al. 2014; Fiore et al. 2017), which make it an excellent target to investigate the complex interplay between outflow and star formation in the intensest case. As an analog of the high-z luminous HyLIRGs/quasars (e.g., Harrison et al. 2012; Perrotta et al. 2019), J1126 at a lower redshift provides the opportunity to understand the evolution of those high-z galaxies with a higher S/N and spatial resolution (e.g., 6 kpc per arcsec at z = 0.5 vs. 8.5 kpc per arcsec at z=2).

The paper is organized as follows. The reduction of the Gemini and ALMA observations are described in Section 2. The analyses of the Gemini data including the spatially-resolved kinematics of ionized gas as well as the association between outflow and gas ionization, are reported in Section 3. The analyses of the ALMA observations, e.g., the identification of molecular outflow, are reported in Section 4. In Section 5 we discuss the dynamical properties, the driving mechanisms, and the feedback effects of the multi-phase outflows. The results of the analyses are summarized in Section 6. We adopt the cosmological parameters $H_0 = 69.32$ km s⁻¹ Mpc⁻¹, $\Omega_{\rm M} = 0.29$ and $\Omega_{\Lambda} = 0.71$ (Hinshaw et al. 2013) throughout the paper.

2. DATA REDUCTION

2.1. Gemini-N/GMOS IFU observations

J1126 was observed by Gemini-N/GMOS in 2021 March (ID: GN-2020B-Q-117, PI: Chen). The observation was conducted with a total of 2 hours on-source exposure in two nights in the 2-slit IFU mode of GMOS. The 2-slit IFU mode has a field of view (FoV) of $5'' \times 7''$,



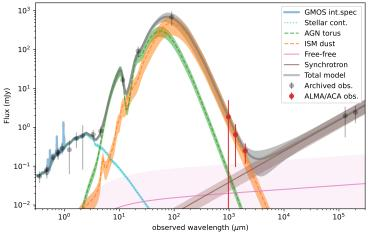


Figure 1. Left: HSC gi-composite image of J1126 and a nearby faint galaxy, J1126b. J1126 was observed by HSC only in the two bands. The PSF and FoV of the GMOS observation are shown in blue circle and dotted rectangle, respectively. The orange ellipse denotes the beam of the Band 4 observation of ALMA. Right: Archived data (grey dots) and the new ALMA observations of continua (red dots) of J1126 with the best-fit SED fitting results. The error bars show $\pm 3\sigma$ errors, which are the original measurement errors plus 10% of the fluxes to account for the systematic errors among instruments. The GMOS spectrum is shown in blue. The total best-fit model is shown in the grey curve with $\pm 3\sigma$ uncertainty range in the grey shadow region. All of the fitting components with their $\pm 3\sigma$ uncertainties are also shown with the markers denoted in the legend. See details of the archived observations in Section 2.4 and the SED fitting in Section 4.1.

which is set to cover J1126 and a faint companion galaxy (Figure 1, left panel). The Point Spread Function (PSF) of the IFU data is estimated with the size of stars, $\sim 0.7''$, in acquisition images taken in i-band ($\sim 7500\mbox{\normalfont\AA}$) and the wavelength-dependent relation, $\propto \lambda^{-1/5}$, of the Kolmogorov turbulence model (e.g., Fried 1965; Roddier 1981). The grating R150 was utilized to achieve a wide wavelength coverage, i.e., from [OII] 3729Å line to [SII] 6731Å line, which provides a spectral resolution of R $\sim 1000~(\sim 300~\mbox{km}\,\mbox{s}^{-1})$ around 7000Å. The wavelength accuracy estimated with night sky emission lines is $\sim 50~\mbox{km}\,\mbox{s}^{-1}$.

The GMOS data is reduced with the Gemini IRAF package (Gemini Observatory & AURA 2016), e.g., to calibrate the wavelength, mask bad pixels, remove the scattered light, correct for the atmospheric dispersion, and subtract the night sky emissions. The cosmic rays are rejected with the L.A.Cosmic algorithm (van Dokkum 2001). The atmospheric extinction is corrected with the extinction curve at Mauna Kea (Buton et al. 2013). The Galactic extinction is corrected with the extinction curve of Cardelli et al. (1989) and the Galactic dust reddening map of Schlafly & Finkbeiner (2011). The standard star Feige 34 was observed with the same configurations as those of the observation of J1126 to derive the spectral response curve of the instruments; we also utilize the observation of a red star KF08T3 from the program (ID: GN-2022A-Q-221, PI: Chen) to reduce the contamination of the 2nd-order spectrum in the derivation of the response curve. The spectra of J1126 is corrected with the response curve and then calibrated with the SDSS photometry in the r', i', and z' bands,

which are fully covered by the GMOS observations. Images are created by convolving the GMOS cube with the SDSS transmission curves of these bands and used to calculate the magnitudes with a de Vaucouleurs profile; the derived magnitudes are then compared to SDSS model magnitudes (based on the same profile) to obtain the calibration factor. These image are also used to derive the absolute astrometry of GMOS data by matching the intensity centers of them to those in the corresponding SDSS images of J1126.

With the adopted configuration using R150, the (1st-order) spectra of the GMOS blue-slit can be contaminated by the 0th-order spectra of the GMOS red-slit in the range of rest 4370Å–4420Å (as shown in Figure 2), which is masked out in the later analyses.

2.2. ALMA observations

J1126 has been observed by ALMA in Band 4 and 6 for the detections of CO(2-1) and CO(3-2) emission lines with rest frequencies of 230.538 and 345.796 GHz , respectively. The Band 4 observation was conducted in Cycle 8 (project ID: 2021.1.01496.S, PI: Chen) in an extended array configuration with baselines from 41.4 to 3396.4 meters that yields a mean angular resolution (AR) of 0.17"and and a maximum recoverable scale (MRS) of 2.4", plus a compact array configuration with baselines from 14.9 to 876.6 meters that yields a mean AR of 0.69"and and a MRS of 7.6". The achieved sensitivity is 0.06 and 0.13 mJy beam $^{-1}$ over 100 km s $^{-1}$, for observations with the extended and compact arrays, respectively. The Band 6 observation was conducted in Cycle 9 (project ID: 2022.1.01376.S, PI: Chen) in an ex-

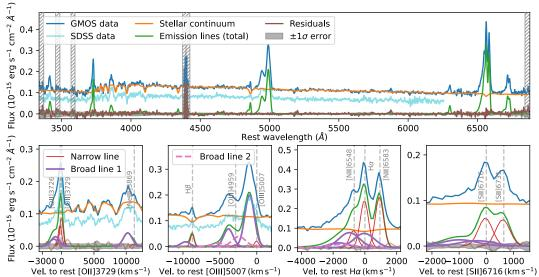


Figure 2. Top: Integrated GMOS spectrum of J1126 (blue) with the best-fit stellar continuum (orange) and emission lines (green). The fitting residuals are shown in brown and the $\pm 1\sigma$ error range in grey shadow region. The grey hatched regions denote the wavelength ranges with large instrumental errors, which are masked out in the fitting. The SDSS spectrum of J1126 is shown in cyan for a reference, which is fainter than the GMOS spectrum due to a small aperture. Bottom: Zoom-in windows of [OII] doublets and [NeIII] (left), Hβ and [OIII] doublets (middle-left), Hα and [NII] doublets (middle-right), as well as [SII] doublets (right). The grey vertical lines represent the rest wavelengths of these lines. The red thin lines show the best-fit narrow line profiles; the violet lines show the broad line profiles for each line, while the purple dashed lines show the additional broad profiles for [OIII], Hα, and [NII]. The x-axis is converted to velocity in relative to the rest wavelengths of [OII] 3729Å, [OIII] 5007Å, Hα, and [SII] 6716Å, respectively, in the four panels. Other legends are the same as those in the top panel.

tended array configuration with baselines from 79.4 to 5323.0 meters that yields a mean AR of 0.09"and and a MRS of 1.0". The sensitivity of the Band 6 observation is 0.18 mJy beam $^{-1}$ over 100 $\rm km\,s^{-1}$.

The Band 4 and 6 data sets are calibrated using CASA¹ and the pipeline scripts delivered by ALMA. In order to maximize the uv coverage, we combine the Band 4 observations with the extended and compact arrays with the CASA task concat with the default weight in the calibrated measurement sets. The continuum in the Band 4 and 6 data sets is subtracted in the uv plane using the CASA task uvcontsub_old² in line-free frequency ranges. The continuum-subtracted visibilities are then deconvolved utilizing the CASA task tclean with the weighting option of Briggsbwtaper and a robust number of 0.5. The reduced Band 4 and 6 data sets have synthesized beams of $0.20'' \times 0.16''$ with a position angle (PA) of 331° , and $0.12'' \times 0.09''$ with a PA of 323° , respectively.

In order to perform a direct comparison between observations of the two CO lines, e.g., to derive the line ratio, we create modified CO(2-1) and CO(3-2) cubes with matched beams and MRS. The modified CO(2-1)

cube is obtained via a cut of the visibilities with baselines shorter than 119.1 meters, i.e., to reduce the MRS. The modified CO(3-2) cube is obtained via a Gaussian taper, $0.14'' \times 0.09''$ with a PA of 350°, in the tclean process. The consequent modified cubes have a synthesized beam of $0.20'' \times 0.16''$ (1.2×1.0 kpc) with a PA of 331°, and a MRS of $\sim 1.0''$ (6.0 kpc).

In addition to the CO line image cubes, we also create the continuum images in Band 4 and 6 (1340 and 890 μ m in the rest frame) with the data sets in line-free frequency ranges using tclean in a MFS mode with a weighting option of Briggs and a robust number of 0.5.

J1126 was also observed by Atacama compact array (ACA) in Band 7 in Cycle 7 (project ID: 2019.2.00085.S, PI: Chen) with a sensitivity of 2.43 mJy beam ⁻¹ over 100 km s⁻¹. The Band 7 continuum and CO(4-3) line (461.041 GHz in rest frame) are reduced following similar processes as done for Band 4 and 6 data sets. The mean AR of the ACA observation is 4.9"(29 kpc), i.e., J1126 is unresolved in the observation, and we only use the spatially integrated continuum and CO(4-3) line in the analyses.

2.3. Definitions of the systemic redshift and the position of the galaxy center

In order to perform a self-consistent analysis for GMOS and ALMA observations, we adopt uniform definitions of the systemic redshift and the position of the galaxy center throughout the paper. The sys-

¹ Common Astronomy Software Applications (McMullin et al. 2007).

² We use the old version of uvcontsub since the current version does not support fitting across multi spectral windows.

temic redshift of the galaxy can be estimated from the absorption features in stellar continuum (GMOS) and the narrow components of CO emission lines (ALMA). Throughout the paper we adopt the systemic redshift, 0.468417 ± 0.000002 , measured from the CO(2-1) emission in the central region ($r{<}0.5$ kpc; Section 4.2), which shows a higher accuracy than those from the stellar continuum fitting, 0.4685 ± 0.0001 (Section 3.1). The difference between the two estimates is within the uncertainty of GMOS wavelength calibration ($\sim 50~{\rm km\,s^{-1}}$).

The position of the galaxy center can be estimated with intensity maps of stellar continuum (GMOS), dust continuum, and CO emission lines (ALMA). Throughout the paper we adopt the galaxy center as the center of the CO(2-1) intensity map (Section 4.2), $11^{\rm h}26^{\rm m}57^{\rm s}.771 + 16^{\rm d}39^{\rm m}11^{\rm s}.79$, which is estimated with a two-dimensional Gaussian fitting and has an angular accuracy of $\sim 0.01''$ under the array configuration. The Band 4 dust continuum has the same center as CO(2-1). The center of the stellar continuum in V-band (Section 3.1) has a relative distance of 0.1" from the center of CO(2-1), which could be due to the positional uncertainty of GMOS ($\sim 0.1''$) and SDSS ($\sim 0.1''$, for astrometric calibration).

2.4. Archived observations

We collect the multi-wavelength archived observations of J1126 of the following telescopes: SDSS (u' to z' bands), Subaru/HSC (g and i bands), 2MASS (J, H, and K_s bands), WISE (3.4, 4.6, 12, and 22 μ m), AKARI (90 μ m), and VLA (13 and 20 cm). The integrated fluxes in each band are shown in Figure 1 (right panel). An updated multi-band spectral energy distribution (SED) fitting using the archived data and the new ALMA observations in (sub-)millimeter bands are discussed in Section 4.1.

There is a companion galaxy (J1126b), in the southeast of J1126 with a distance of 3" (Figure 1, left panel). J1126b is faint with an HSC *i*-band magnitude of 19.8. GMOS observation of J1126b results in z=0.1998 from H α line, suggesting that it locates in the foreground of J1126. The spectral fitting for J1126b (see the method in Appendix A) reveals a stellar mass of $2.6 \times 10^9~M_{\odot}$ with a SFR of $0.6~M_{\odot}~\rm yr^{-1}$, i.e., it is not an active star-forming galaxy. Non-detection of [OIII] line suggests no AGN in J1126b. In addition, J1126b is not detected in the ALMA observations in Band 4 and 6. Therefore, the contribution of J1126b in the unresolved IR/radio observations (e.g., WISE and VLA) can be considered to be negligible in the later analyses (e.g., SED fitting of J1126).

3. ANALYSIS METHOD AND RESULTS OF THE GMOS IFU OBSERVATIONS

J1126 is identified as a Type-2 AGN since there is no features of Type-1 AGNs in its optical spectra (e.g., extremely broad permitted lines, Balmer continuum, and iron pseudo continua; Chen et al. 2020b). We fit the GMOS spectra using the PopStar stellar templates (Millán-Irigoyen et al. 2021) plus Gaussian profiles for emission lines. Two Gaussian profiles are used to fit each line, in which a narrow profile with a full-width-half-maximum (FWHM) < 700 km s⁻¹ reflects the line emitting from gas on the galaxy disk, and a broad line profile (FWHM > 700 km s⁻¹) indicates the line emitting from the outflowing gas. An additional broad component with a velocity shift $(v_s) < -2000 \text{ km s}^{-1}$ is required for the bright blueshifted wings of [OIII] doublets and $\text{H}\alpha$ -[NII] complex. The spectral fitting is performed for each pixel of the original GMOS data cube. Details on the fitting method are described in Appendix A.

The GMOS data shows a moderate resolution, $\sim 0.7''$ (4 kpc). If J1126 has a compact outflow (e.g., < 1kpc; Genzel et al. 2014; Carniani et al. 2015), it can be blurred by the PSF and observed to be extended. On the other hand, the highly-blueshifted [OIII] line profile (Figure 2) suggest a face-on view of the ionized outflow. Even if the outflow is intrinsically extended, it could show a bright core component in the galaxy center where the line of sight is close to the central axis of the outflow cone. In addition, it is reported that ULIRGs usually have compact starburst nuclei, which have a typical size of ~ 100 pc and contribute the bulk of the star formation in the host galaxy (e.g., Privon et al. 2017; Falstad et al. 2021; García-Bernete et al. 2022). Such bright core components of outflows and star formation could dominate the observation, while the emission in the outskirt could be hidden. In order to determine whether the outflow in J1126 is indeed extended, and investigate the properties (e.g., kinematics and ionization of gas) in the galaxy outskirt to understand the feedback effect of outflow on the entire galaxy, we also perform the spectral fitting for the cube after removing an unresolved core component. The core component is obtained using the wavelength-dependent PSF with its peak scaled by the mean spectrum of the central pixels within $\sim 0.2''$. The core component contributes to 60%, 42%, and 36% of the total fluxes of the [OIII]-traced outflow, the narrow $H\alpha$ line, and the V-band stellar continuum of the entire galaxy.

The best-fit fitting results of the original and the coreremoved cubes are discussed in the following subsections. The estimation of stellar mass is shown in Section 3.1. The kinematics and ionizing mechanisms of ionized gas are discussed in Section 3.2 and 3.3, respectively. The comparison between the extinction estimated from the stellar and nebular emission is discussed in Section 3.4.

3.1. Properties from the stellar continuum

An integrated spectrum is extracted within a radius of 1.5" (9.0 kpc) and used to estimate properties of the entire galaxy. The best-fit result for the integrated spectrum is shown in Figure 2, in which the stellar continuum

is marked in orange. The continuum fitting is performed with an non-parametric star formation history (SFH; e.g., Hernandez et al. 2000) and the PopStar templates. We assume the initial mass function of Kroupa (2001) and a fixed solar metallicity. The best-fit SFH from the integrated spectrum consists of an old stellar population with ~ 1 Gyr and a starburst in the recent several tens Myr³. The total stellar mass (M_{\star}) is estimated to be $(2.0 \pm 0.5) \times 10^{11} \ M_{\odot}$ after corrected for the remaining mass fraction provided by the PopStar model. The bestfit stellar continuum has a velocity dispersion (Δv_{σ}) of $343 \pm 21 \text{ km s}^{-1}$, which is estimated with the absorption features (e.g., H- and K-lines of calcium around rest 4000Å) and corrected for the instrumental broadening (FWHM $\sim 300 \; \mathrm{km} \, \mathrm{s}^{-1}$). The estimated M_{\star} and Δv_{σ} are consistent with the Faber–Jackson M_{\star} - Δv_{σ} relation observed in massive galaxies (e.g., Barat et al. 2019).

In the stellar continuum fitting, it is assumed that old stars and young stars that migrate from the dense birth clouds, i.e., in the diffuse interstellar medium (ISM), suffer the same amount of extinction. The best-fit SFH under the assumption suggests that the recently formed stars, which is younger than 30 Myr and older than the birth clouds timescale (e.g., 6 Myr; Kennicutt et al. 2009), contribute to 98% of the stellar ionizing flux in the diffuse ISM and 85% of the observed stellar continuum flux in V-band. The map of the V-band stellar continuum is obtained by integrating the best-fit stellar continuum (before extinction correction) with the V-band transmission curve in the rest frame (Figure 3). The intensity map has an effective radius (i.e., the half-light radius) of 3.0 kpc (0.5'') after correction for the PSF. The stellar light is more extended towards the north as shown in the core-removed intensity map, which suggests an intense recent star formation in the north. The dust extinction $(A_{V, \text{stellar}})$ from the stellar continuum fitting is shown as contours in Figure 3. The extinction is higher in the south in both of the original and coreremoved maps, which is probably associated with the dust carried out from the nuclear dusty region by the outflow. We discuss the relative contribution of young stars and the AGN on gas ionization in Section 3.3; and compare the extinction estimated from stellar continuum and nebular emission in Section 3.4.

3.2. Kinematics of ionized gas

Thanks to a wide wavelength coverage of the GMOS observations, a series of emission lines are detected including transitions of ions with low ionization potential (IP, e.g., < 15 eV), i.e., the hydrogen Balmer lines, [OII] 3729Å, [NII] 6583Å, and [SII] 6716,6731Å doublets; high-IP ionized lines (e.g., IP > 30 eV), i.e.,

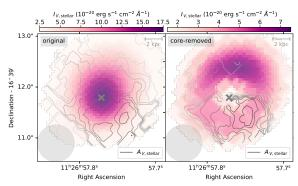


Figure 3. Intensity maps of the rest V-band stellar continuum from the original (left) and core-removed (right) GMOS data. The grey contours show the extinction estimated from the fitting of stellar continuum. Only pixels with V-band S/N > 5 are shown in the panels. PSF is shown in grey circles and the galaxy center in grey crosses.

[OIII] 5007Å, [NeIII] 3869Å, and [NeV] 3426Å; and an emission line of the neutral atomic oxygen, [OI] 6300Å. The kinematic properties of the emission lines are reported in this subsection.

The best-fit narrow and broad line components for the GMOS integrated spectrum are shown in Figure 2 (bottom panels). Each of the kinematic components are fixed to the same shift velocity ($v_{\rm s}$) and FWHM in the fitting for each emission line. The narrow component has a $v_{\rm s}$ of -33 ± 3 km s⁻¹ and a FWHM of 530 ± 10 km s⁻¹, while the (primary) broad component has a $v_{\rm s}$ of -980 ± 20 km s⁻¹ and a FWHM of 1460 ± 40 km s⁻¹. Those two components are used for each emission line. An additional broad component is required to fit the broad wings of [OIII] doublets and H α -[NII] complex (Figure 2, bottom-middle panels), which has a more blueshifted profile with a $v_{\rm s}$ of -2410 ± 160 km s⁻¹ and a FWHM of 2080 ± 220 km s⁻¹. The line widths have been corrected for the instrumental broadening of GMOS observation (~ 300 km s⁻¹).

The flux fraction of the broad components over the entire line profile (f_{broad}) has been calculated for each emission line. We also calculate the 50th percentile velocity (v_{50}) and the line width $(\Delta v_{80} = v_{90} - v_{10})$ with the best-fit line models, as the kinematic parameters of the entire profile of each line. For instance, [OIII] 5007Å has a predominant broad component that contributes to 97% of its total flux with $v_{50} = -1210 \pm 10 \text{ km s}^{-1}$ and $\Delta v_{80} = 2370 \pm 40 \text{ km s}^{-1}$, which provides an excellent tracer of the ionized gas outflow. The other high-IP lines, i.e., [NeIII] and [NeV], also have a f_{broad} over 90%, indicating that they are mainly emitted from the outflowing gas. On the contrary, the low-IP lines, e.g., [OII], and $H\alpha$, have a relatively low f_{broad} of $\sim 40\%$, suggesting a mixed contribution of emission by gas in the outflow and in the galaxy disk. The detailed values of the kinematic parameters for each emission line are listed in Table B2.

³ Details of the SFH estimated with the stellar continuum and other estimators are discussed in Appendix D.

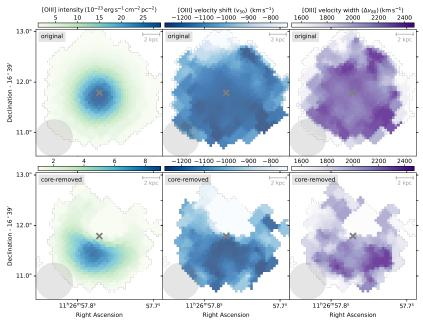


Figure 4. Top: Intensity (left), velocity shift (v_{50} , middle) and width (Δv_{80} , right) maps of [OIII]. Only pixels with S/N > 3 for [OIII] flux are shown. PSF is shown in grey circles and the galaxy center in grey crosses. Bottom: The same as the top panels for the core-removed GMOS data.

We then investigate the spatial distribution of intensity and kinematics of these emission lines. Figure 4 shows maps of intensity (before correction for intrinsic extinction), velocity shift (v_{50}) and velocity width (Δv_{80}) of the tracer of the ionized outflow, [OIII] 5007Å, for both of the original and core-removed data cubes. The original intensity map has a PSF-corrected effective radius of 1.5 kpc. The intensity maps, especially the core-removed one, show a spatial distribution tilted to the south. The velocity maps indicate the fast outflow (i.e., high v_{50} and Δv_{80}) is extended to the southern outskirt region ($\sim 3 \text{ kpc}$). The other high-IP lines, [NeIII] and [NeV] have a similar south-tilted morphology (Figure B1). We discuss the dynamical properties of the outflow (e.g., the mass-loss rate) and its feedback effect in Section 5.

Unlike [OIII] that is dominated by the outflow, the low-IP lines, e.g., $H\alpha$, have a mixed contribution of both of the fast outflow and the narrow line component. The intensity maps of the narrow and broad components of $H\alpha$ are shown in Figure 5 (left panels). The effective radii of the narrow and broad components are 2.4 and 1.2 kpc, respectively, after correction for the PSF blurring. The broad component shows a south-tilted distribution, which is similar to [OIII] and suggests the outflowing hydrogen and oxygen gas locate in the same region⁴. The narrow $H\alpha$ line has a different distribution, which is more extended to the north, i.e., opposite

to the outflow, in the core-removed map. The velocity shift maps of the narrow $H\alpha$ line show a pattern of a rotating disk. Interestingly, although the velocity FWHM of the narrow H α line (300–600 km s⁻¹) is only 1/5– 1/3 of those of the fast outflow components, it shows an increasing trend towards the direction of the fast outflow (e.g., the bottom-right panel of Figure 5). This enhanced dispersion along the outflow direction suggests a strong effect of the fast outflow on the disk gas, e.g., with a large opening angle or an orientation close to the disk plane. The intensity maps of the other low-IP lines and the atomic oxygen line are shown in Figure B2 and B3. All of these lines have a broad component towards the south, i.e., following the direction shown by the fast [OIII] outflow. However, their narrow component show different morphologies: $H\beta$ extended to the north, i.e., similar to $H\alpha$; while the intensity of [NII], [OI], and [SII] is enhanced in the southern region. The different morphologies suggest different mechanisms of gas ionization with their ratios, which will be discussed in Section 3.3.

3.3. Mechanisms of gas ionization

We use the line ratio diagnostics to understand the energy source of gas ionization in the galaxy, which is the so-called BPT diagrams (Baldwin et al. 1981; Kewley et al. 2001; Kauffmann et al. 2003). The predominant broad component of the bright [OIII] line results in an extremely high [OIII]/H β ratio, i.e., $\log (f_{[OIII]}/f_{H\beta}) = 1.16 \pm 0.02$ in the broad component of the GMOS integrated spectrum, which corresponds to the maximum value of the local SDSS galaxies (Kewley et al. 2006). The broad line ratios of J1126 locate in the typical AGN/Seyfert regions in the BPT diagrams (Figure 6),

⁴ The broad component of H α could have a large uncertainty in the faint outskirt region due to the blurring of the adjacent broad [NII] lines. See discussion in Appendix B.1.

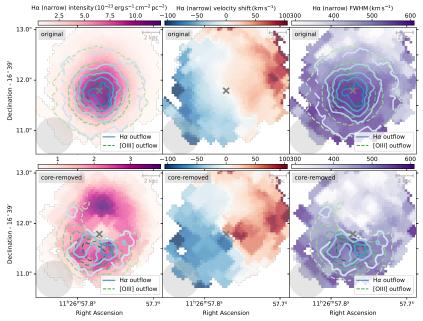


Figure 5. Top: Intensity (left), velocity shift (v_s , middle) and width (FWHM, right) maps of narrow component of Hα line. The [OIII] outflow intensity is also shown in green dashed contours to indicate the alignment between the outflows traced by Hα and [OIII]. The shown velocity shift in the middle panel is in relative to the best-fit v_s of narrow line of the integrated spectrum, which has a shift of -33 km s^{-1} for v_s in relative to systemic velocity using CO(2-1) (Table A1). An S/N > 3 cut is used for the narrow Hα line maps and the contours of Hα and [OIII] outflows. PSF is shown in grey circles and the galaxy center in grey crosses. Bottom: The same as the top panels for the core-removed GMOS data.

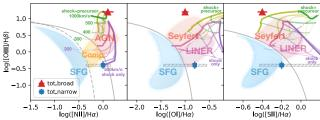


Figure 6. [OIII]/H β vs. [NII]/H α (left), [OI]/H α (middle), and $[SII]/H\alpha$ (right) ionization diagrams with the emission line ratios of narrow (blue) and broad (red) components of integrated spectrum of J1126. The solid and dashed line represents the classification lines of Kewley et al. (2001) and Kauffmann et al. (2003), respectively. The dot-dashed lines in the middle and right panels represent the empirical classification line of Seyferts and LINERs by Kewley et al. (2006). The range of SDSS galaxies with types of SFG (blue), composite (yellow), AGN/Seyfert (red), and LINER (violet) are denoted in the filled regions (Kewley et al. 2006). The shock+precursor models with velocity of 300–1000 km s⁻¹ (green) and magnetic field intensity of 10^{-4} – $10 \mu G$ (yellowgreen), as well as the shock-only models with $200-500 \text{ km s}^{-1}$ (violet) and 10^{-4} – $10 \mu G$ (purple), are shown as grids (thicker lines for higher values) adopting the solar abundance and a preshock density of 1 cm⁻³ (Allen et al. 2008). The horizontal hatches show the ranges of color bars in Figure 7.

suggesting a significant of contribution of AGN radiation on the ionization of the outflowing gas. The high $[OIII]/H\beta$ ratio can also be explained by a fast shock as the fast outflow (i.e., 1000 km s⁻¹) penetrates into the ambient ISM in the outer regions of the galaxy. As the shock velocity increases, the cooling of hot gas behind the shock front generates a strong radiation field of extreme UV and soft X-ray photons, and produces a supersonic photoionization front that moves ahead of the shock front and pre-ionizes the gas, which is the socalled photo-ionizing precursor (e.g., Allen et al. 2008; Kewley et al. 2013). The shock+precursor models of Allen et al. (2008) are shown as green grids in Figure 6. The precursor can make a significant contribution to the ionized gas emission lines such as [OIII] 5007Å (e.g., Santoro et al. 2018). Since J1126 possesses a luminous AGN (e.g., bright AGN radiation in mid-IR) and a fast, extended outflow, there could be a mixed contribution of the direct AGN radiation and the shock precursor on the ionization of the outflowing gas. Such a mixture of ionization mechanisms in outflows of several nearby quasars is reported in Hinkle et al. (2019).

On the other hand, the narrow lines of the integrated spectrum show a moderate [OIII]/H β ratio, i.e., $\log (f_{\rm [OIII]}/f_{\rm H}\beta) = -0.35 \pm 0.11$, due to the faintness of narrow [OIII] line. The narrow line ratios locate in the composite region in the [NII]/H α diagram, the lowinoization narrow emission line regions (LINER) in the [OI]/H α diagram, and the star formation region in the [SII]/H α diagram (Figure 6), suggesting a mixed con-

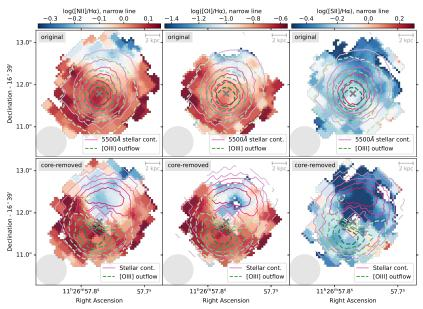


Figure 7. Maps of [NII]/H α (left), [OI]/H α (middle), and [SII]/H α (right) of narrow lines from the original (top) and coreremoved (bottom) GMOS data. The bounds of color bar of [NII]/H α maps are set as the boundaries of the composite ionization (Figure 6, left) with log ($f_{[OIII]}/f_{H\beta}$) = -0.35 from the integrated spectrum. The ranges of color bars of [OI]/H α and [SII]/H α maps are also shown in Figure 6. In all of the maps, a bluer color denotes a larger contribution of star formation and a redder color shows a larger contribution of shock. Only pixels with S/N > 3 for both of the two lines to derive the ratios are shown in the panels. The distributions of V-band stellar continuum and [OIII] outflow are shown in purple solid and green dashed contours, respectively, to indicate the associations of them to different ionizing mechanisms. PSF is shown in grey circles and the galaxy center in grey crosses.

tribution of LINER and star formation ionization. The power sources of LINER include inefficiently accreting low-luminosity AGN (LLAGN), shock, and aged stars in post-starburst galaxies (Kewley et al. 2013, and references therein). Since J1126 is a starburst galaxy with a luminous AGN, a low-speed shock (i.e., without the supersonic precursor), which are shown as violet grids in Figure 6, can be the most likely ionization mechanism (e.g., Allen et al. 2008; Rich et al. 2010). Therefore, the narrow lines of J1126 (i.e., gas on the galaxy disk) can be ionized by a combination of starburst and shock mechanisms.

We use the maps of line ratios to determine the ionizing mechanisms in the galaxy disk. The map of line ratios, $[NII]/H\alpha$, $[OI]/H\alpha$, and $[SII]/H\alpha$ are shown in Figure 7 for both of the original and core-removed IFU data. Since the narrow [OIII] line is faint, we assume a common $[OIII]/H\beta$ ratio from the integrated spectrum, i.e., $\log (f_{\text{[OIII]}}/f_{\text{H}\beta}) = -0.35$, for the entire galaxy. The color bars of the maps are set with the adopted $[OIII]/H\beta$ ratio and the boundary equations of different ionizing mechanisms of Kewley et al. (2001) and Kauffmann et al. (2003). In all of the maps, a bluer color indicates an increasing contribution from star formation activity, while a redder color indicates an increasing contribution from LINER (mainly due to shock, as discussed above). The [NII]/H α and [OI]/H α maps indicate that the ionization in the south is mainly contributed by shock whereas star formation dominates ionization in the northern region. The star formation ionization in the north is more apparently exhibited in the core-removed maps. Similar to [NII]/H α and [OI]/H α , the [SII]/H α map also shows a star formation dominated ionization in the north and an increasing trend towards the south. Although the line ratio in the south, $\log f_{\rm [SII]}/f_{\rm H}\alpha \sim -0.2$, is still in the regime of star formation ionization with the classification of Kewley et al. (2001), recent studies report that such ratio can be produced by shock excitation in supernova remnants or outflow (e.g., Kopsacheili et al. 2020). To summarize, the maps of [NII]/H α , [OI]/H α , and [SII]/H α suggest a stronger star formation ionization in the northern outskirt of J1126, and a larger contribution by shock ionization towards the south.

The maps of narrow line ratios are also compared to the spatial distribution of the stellar continuum and the fast [OIII] outflow (contours in Figure 7). A tight association is exhibited in the core-removed maps: the star formation ionization is related to the stellar light from young stars in the north; and the shock ionization is aligned with the distribution of fast outflow in the south. The association between shock ionization of the disk gas and the fast outflow implies that the ionizing shock could be related to the large gas dispersion (e.g., Arp 220, Perna et al. 2020) in the galaxy disk, which is promoted by the fast outflow (Section 3.2; Figure 5, bottom-right panel). It is also possible that the disk gas is ionized by diffuse ionizing photons from the shock precursor of the fast outflow along its orientation. Either of

the mechanisms indicates a significant effect of the fast outflow on the gas ionization in the disk.

The intensity map of the broad $H\alpha$ line exhibits a cavity in the south outflow region (Figure 5), where the broad [OI], [NII], and [SII] lines show enhanced intensity (Figure B3 and B5). These results could suggest strong shock in the outflowing gas as implied by the integrated broad line ratios (Figure 6). However, a spatially-resolved line ratio diagnostics is not applicable due to the large uncertainty of the decomposition of broad $H\alpha$ and [NII] lines in faint outskirt region. A detailed discussion on the fitting uncertainty is shown in Appendix B.1.

3.4. Dust attenuation estimated with stellar and nebular observations

With the integrated spectrum, the dust attenuation of the stellar radiation is estimated to be $A_{V,\text{stellar}} =$ 1.5 ± 0.1 via the spectral fitting of the continuum. The extinction of the nebular region is $A_{V, \, \rm narrow} = 3.0 \pm 0.2$ for the galaxy disk and $A_{V,\,\mathrm{broad}}=1.7\pm0.5$ for the gas in outflow, which are estimated using the Balmer decrement of the narrow and broad components, respectively. All of the estimations follow the extinction curve of Calzetti et al. (2000) with $R_{\rm V}=4.05$. An intrinsic $H\alpha/H\beta$ ratio of 2.86 from Case B recombination with an electron temperature of 10⁴ K and an electron density of 100 cm^{-3} (Storey & Hummer 1995) is used to estimate the nebular extinction. The ratio is usually adopted as the intrinsic value in star-forming regions (e.g., Battisti et al. 2017) and is also used in outflow studies (e.g., Fiore et al. 2017). A higher $H\alpha/H\beta$ ratio, 3.1, is employed for AGNs in the literature due to enhanced collisional excitation of H α (e.g., Ferland & Netzer 1983; Veilleux et al. 1995). Since it is difficult to quantitatively separate the contributions of star-forming region and the AGN in gas ionization, we adopt a single ratio, 2.86, in the analysis. Lower extinction values, i.e., $A_{V, \text{narrow}} = 2.7$ and $A_{V, \text{broad}} = 1.4$, can be derived if 3.1 is adopted.

The nebular region on the disk is more obscured than the stellar light with a stellar-to-nebular (disk) attenuation ratio of $A_{V, \text{stellar}}/A_{V, \text{narrow}} = 0.5 \pm 0.1$, which is similar to the typical value, 0.44, reported by Calzetti (1997). The attenuation ratio is found to be correlated with several properties of galaxies, e.g., M_{\star} , SFR, and metallicity, in recent works (e.g., Koyama et al. 2019; Lin & Kong 2020; Li et al. 2021). A two-component dust model is usually adopted to explain the differences between $A_{V, \text{ stellar}}$ and $A_{V, \text{ narrow}}$ in star-forming galaxies (e.g., Charlot & Fall 2000). In this model, the massive young stars are embedded in dense birth clouds while the long-lived stars locate in less-obscured diffuse ISM. Massive young stars can provide the bulk of the ionizing photons. For example, under the assumption of a constant SFR in the recent 100 Myr with the PopStar templates, stars younger than 6 Myr (i.e., lifetime of O-type stars, Kennicutt et al. 2009; Calzetti 2013) contribute to 96% of the total ionizing flux in star-forming region. Therefore the $A_{V,\,\mathrm{narrow}}$ based on Balmer lines can trace the attenuation of radiation of young stars that travels through the dense birth clouds and the outside diffuse ISM. Since the radiation from the young stars can be highly obscured, the observed stellar light can be dominated by the long-lived stars that only suffer the extinction of the less-obscured diffuse ISM. As a consequence, the continuum-based $A_{V,\,\mathrm{stellar}}$ mainly traces extinction in the diffuse ISM. For example, with the estimated $A_{V,\,\mathrm{narrow}}=3.0,\,A_{V,\,\mathrm{stellar}}=1.5$ and the above assumption of constant star formation, 96% of the observed V-band stellar continuum is emitted by the long-lived stars (t>6 Myr) in the diffuse ISM.

The dust extinction in J1126 can be more complicated than pure star-forming galaxies due to a significant contribution of AGN/shock in ionization, and a possible foreground extinction by the dust entrained in the extended outflow. Following a similar assumption of the two-component dust model of star-forming galaxies, we consider that the measured $A_{V, \text{stellar}}$ reflects the extinction of diffuse medium, which can be a mixture of the extinction of the host diffuse ISM and that of the dust entrained in the outflow. The pure extinction in obscured ionizing regions $(A_{V, \text{ionizing}})$ either by young stars or shocks in the host disk can be estimated by removing the foreground extinction (e.g., by dust in diffuse ISM or outflow) from the values based on the Balmer decrement, i.e., $A_{V, \text{ionizing}} = A_{V, \text{narrow}} - A_{V, \text{stellar}}$. The maps of these estimates are shown in Figure 8.

Both of the original and the core-removed maps of $A_{V,\,\rm stellar}$ show an increasing trend towards the south. The enhanced extinction in the south is associated with the fast ionized outflow, suggesting that the enhancement is probably due to the dust carried out by the outflow from the dense central region that shields the underlying stellar light in the southern outskirt. The difference of $A_{V,\,\rm stellar}$ between the south (with outflow, ~ 1.0) and north (no outflow, ~ 2.5), ~ 1.5 , is similar to the extinction of the outflowing gas, $A_{V,\,\rm broad}=1.7$, estimated from the integrated spectrum, which supports the explanation of dust entrained in the outflow.

The original map of the pure extinction in ionizing regions shows $A_{V, \text{ionizing}} = 2.0\text{--}3.0$ in the central region of the galaxy, which suggests the heavy obscuration of the central starburst and/or the AGN/shock-ionizing region. In the core-removed map, the high $A_{V, \text{ionizing}}$ (~ 2.5) is mainly shown in the north where star formation dominates the ionization (e.g., Figure 7), indicating that the dusty environment is extended from the central starburst to the star forming region in the northern outskirt. The southern shock-dominated region exhibits relatively low extinction $A_{V, \text{ionizing}} \sim 0.5\text{--}2.0$, and implies that the extended shock can occur in gas less-obscured than the dense star-forming clouds.

Due to the faintness of broad H β (Figure B2) and the difficulty to decompose broad H α and [NII] (Ap-

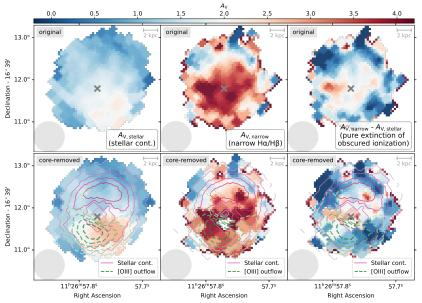


Figure 8. Dust extinction estimated with stellar continuum fitting $(A_{V, \text{stellar}}, \text{left})$, Balmer decrement of narrow lines $(A_{V, \text{narrow}}, \text{middle})$, and the pure extinction of the obscured ionizing region $(A_{V, \text{stellar}} - A_{V, \text{narrow}}, \text{right})$ from the original (top) and core-removed (bottom) GMOS data. The spatial distributions of V-band stellar continuum and [OIII] outflow are shown in the bottom panels to indicate the relation between the extinction and the two components. All of the panels share the same color bar scale. Only pixels with S/N > 5 for V-band continuum and S/N > 3 for both of Hα and Hβ fluxes are shown in the panels. PSF is shown in grey circles and the galaxy center in grey crosses.

pendix B.1) in the outskirt, we do not analyze the map of $A_{V, \text{broad}}$ in this work.

4. ANALYSIS METHOD AND RESULTS OF THE ALMA OBSERVATIONS

4.1. Observations of (sub-) millimeter continua

(Sub-)millimeter continua of J1126 are detected by ALMA at rest 1340 and 890 μ m with a spatial resolution of 1.1 kpc and 0.6 kpc, respectively; and detected at rest 660 μ m by an unresolved ACA observation. The intensity maps at rest 1340 and 890 μ m are shown in Figure 9. The entire flux at 1340 μ m is 0.25 ± 0.02 mJy measured within a radius of 0.7", which is the totalflux-radius from the radial curve of growth. The flux of the continuum at 890 μ m is 0.65 ± 0.12 mJy within a total-flux-radius of 0.2". Since the two total-flux-radii are much smaller than the maximum recoverable scales of the observations i.e., 7.6'' and 1.0'' in 1340 μ m and 890 μ m, respectively, the derived fluxes are considered to reflect the entire fluxes of the galaxy at the two bands. The total flux⁵ at $660 \,\mu\text{m}$, $1.85 \pm 0.87 \,\text{mJy}$, is calculated in a region with a 2×2 beam size of ACA $(15'' \times 9'')$.

The observed (sub-)millimeter continua can be emitted by the dust heated by stellar light, the thermal free-free emission of the ionized gas, and/or the non-thermal synchrotron emission. In order to understand the contribution of these radiation mechanisms, we perform the

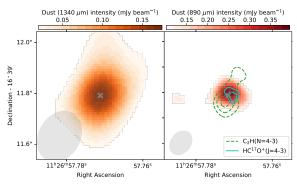


Figure 9. Intensity maps of continua at rest 1340 μ m (left) and 890 μ m (right). The contours in the right panel denote two faint emission lines, i.e., $C_2H(N=4-3)$ in green and $HC^{17}O^+(J=4-3)$ in cyan. The continuum is mainly emitted from the central starburst region (Section 4.1), while the $C_2H(N=4-3)$ line mainly traces the molecular outflow (Section 4.4). Only pixels with S/N>3 are shown for each components, except for $HC^{17}O^+(J=4-3)$ with S/N>2. The beam is shown in grey ellipses and the galaxy center in grey crosses.

SED fitting with the new ALMA observations plus the archived data from optical to radio bands following the method employed in Chen et al. (2020b). The stellar component is constrained by the spectral fitting results reported in Section 3.1. The SKIRTor AGN model (Stalevski et al. 2016) and THEMIS ISM dust model (Jones et al. 2017) are used in the fitting. The free-free and synchrotron components are fit with $S_{\nu} \propto \nu^{-\alpha}$, and the indexes are adopted as $\alpha_{\rm ff} = 0.1$ and $\alpha_{\rm sync} = 0.8$

⁵ The contribution on the flux at $660 \mu m$ by the companion galaxy J1126b is ignorable, since it is not detected the maps of 890 and $1340 \mu m$. There is no other sources in the extracting region.

(e.g., Murphy et al. 2011; Tabatabaei et al. 2017). The best-fit model is shown in Figure 1 (right panel). It is found that the detected continua at 660 and 890 μ m are mainly dominated by the ISM dust radiation (97% and 89%). Synchrotron and free-free emissions contribute to 26% and 10% of the 1340 μ m continuum, respectively.

The spatial profiles of the continua at 890 and 1340 μ m give an half-light radius of 0.2 and 0.3 kpc, respectively, after correction for the beam blurring. The compact dust continuum provides an independent evidence of the highly-obscured central environment as indicated by the nebular attenuation (Section 3.4 and Figure 8).

4.2. Spectra and moment maps of CO emission lines

CO(2-1) and CO(3-2) lines of J1126 are observed by ALMA with different angular resolutions (AR) and maximum recoverable scales (MRS). In order to perform a direct comparison between the two CO lines, we mainly utilize the beam and MRS-matched data cubes (see the reduction in Section 2.2) of CO(2-1) and CO(3-2), which have a mean AR of 1.1 kpc and a MRS of 6.0 kpc, in Section 4.2 and 4.3. The original CO(2-1) cube with a larger MRS (> 40 kpc) is used to estimate the CO flux and molecular gas mass of the entire galaxy; while the original CO(3-2) cube with a higher AR (0.6 kpc) is used to show the detailed outflow structure in the central region (discussed in Section 4.3).

Figure 10 shows the spectra of CO(2-1) and CO(3-2) extracted from the central beam-size region (r < 0.5 kpc) and the disk scale (r < 3 kpc), with the beam and MRS-matched cubes. A multi-gaussian fitting is employed for the CO spectra with a narrow profile for the disk component and one or two wing components for non-circular motion (i.e., 2-Gaussian and 3-Gaussian fit). The velocity of narrow component in the 3-Gaussian best-fit of CO(2-1) in the central region (r < 0.5 kpc) is selected to determine the systemic redshift of the galaxy, $z_{\rm sys} = 0.468417 \pm 0.000002$ (the uncertainty is estimated with Monte Carlo simulations). The broad components that indicates the molecular outflow are discussed in Section 4.3.

We adopt $r_{32} = (S_{\text{CO}(3-2)}/3^2)/(S_{\text{CO}(2-1)}/2^2)$ to calculate the ratios between the two CO lines (e.g., Kirkpatrick et al. 2019; Molyneux et al. 2024; Montoya Arroyave et al. 2024), which is shown in the bottom panels in Figure 10. The spectra of the galaxy disk scale show nearly constant $r_{32} \sim 1$ in the velocity range of $|v_{\rm s}| < 250 \,{\rm km \, s^{-1}}$, which is a bit higher than the average r_{32} of local (U)LIRGs (e.g., 0.8 Montoya Arroyave et al. 2023), and could suggest a stronger heating of starburst in J1126 considering its high SFR of $\sim 800~M_{\odot}\,\mathrm{yr}^{-1}$. The spectra of the central region also show $r_{32} \sim 1$ in the low-velocity range ($|v_s| < 200 \text{ km s}^{-1}$); however, the ratio becomes higher as velocity increases, especially on the blueshifted side where r_{32} even exceeds 3. The relation between high CO excitation and large gas dispersion (e.g., outflow) are reported in several recent works. Cicone et al. (2018) found that the CO(2-1)/CO(1-0) ratio increases in the spatially-resolved outflow of NGC 6240. Montoya Arroyave et al. (2024) reported the CO ladder up to $J_{\rm up}=7$ for 8 local (U)LIRGs with the single-dish APEX observation and found that the components with higher velocity tend to show higher CO excitation (thermalized or over-thermalized line ratios) than the dynamically-quiescent components (sub-thermalized line ratios). The relation between r_{32} and velocity of J1126 suggests the existence of molecular outflow in the central region. We discuss the association between CO excitation and outflow in details in Section 4.3.3.

The maps of intensity, velocity shift and velocity dispersion (i.e., moment-0/1/2 maps) of the beam and MRS-matched cubes of CO(2-1) and CO(3-2) are shown in Figure 11. The intensity maps are integrated within the velocity range of -500 to $500~{\rm km\,s^{-1}}$, which contributes to >99% of the flux of the entire spectral profile (e.g., Figure 10). Both of the two CO lines have a total-flux-radius of $\sim 6~{\rm kpc}$ from the curve of growth, which results in an integrated flux of $6.5\pm0.1~{\rm Jy~km\,s^{-1}}$ for CO(2-1) and $13.1\pm0.7~{\rm Jy~km\,s^{-1}}$ for CO(3-2). The effective (half-light) radii of CO(2-1) and CO(3-2) are 1.0 and 0.6 kpc, respectively. CO(2-1) is more extended than CO(3-2), suggesting a lower CO excitation (e.g.,a lower temperature) in the outside region.

The maps of velocity shift of CO(2-1) and CO(3-2) (middle panels of Figure 11) indicate a pattern of a rotating disk, which has a major axis with a PA of $\sim 280^{\circ}$. The direction of the major axis is estimated to be perpendicular to the direction of pixels with a zero velocity shift. The PA of the molecular gas disk is similar to that of the ionized gas disk as shown in the middle panels of Figure 5. The similar rotating pattern suggests that the (non-outflow) ionized and molecular gas locates in the same disk plane. The velocity dispersion maps of CO(2-1) and CO(3-2) (right panels of Figure 11) both show an enhanced dispersion towards the northwest direction (PA $\sim 340^{\circ}$), suggesting the existence of molecular outflow in this region.

In the above discussions we adopt the MRS-matched CO(2-1) cube for a comparison to CO(3-2) observation, which can loss flux in a large scale, e.g., > 1 kpc. In order to estimate the entire molecular gas mass $(M_{\rm H2})$ of J1126, we employ the original CO(2-1) cube that has an integrated flux of 7.62 ± 0.13 Jy km s⁻¹ within a totalflux-radius of 6 kpc (i.e., the MRS-matched cube has a flux loss of 14%). Assuming the typical value of the CO-to-H₂ factor $\alpha_{CO} = 0.8$ (Downes & Solomon 1998; Carilli & Walter 2013) and the CO(2-1)/CO(1-0) ratio $r_{21} = 1.0$ in nearby ULIRGs (Montoya Arroyave et al. 2023; Molyneux et al. 2024), the total M_{H2} of J1126 is estimated to be $(1.79 \pm 0.03) \times 10^{10} M_{\odot}$ (the uncertainty reflects the measurement error). The estimated $M_{\rm H2}$ corresponds to a molecular gas mass fraction of $M_{\rm H2}/(M_{\star} + M_{\rm H2}) = 8.3\%.$

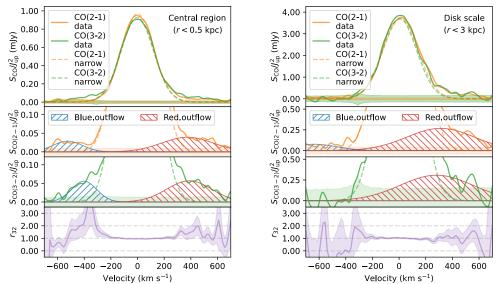


Figure 10. Upper: Continuum-subtracted spectra of CO(2-1) (orange) and CO(3-2) (green) extracted in the central region (r < 0.5 kpc, left) and in a galaxy disk scale (r < 3 kpc, right) with the beam and MRS-matched cubes. The spectra are convolved by a Gaussian profile with FWHM of 50 km s⁻¹. The narrow components of 3-Gaussian fitting are shown in orange and green dashed curves for CO(2-1) and CO(3-2), respectively. The $\pm 1\sigma$ error ranges are denoted in shadow regions. Middle-upper: A zoom-in at the bottom of CO(2-1) profile. The blue- and redshifted outflow components are shown in blue and red hatches, respectively. Middle-lower: A zoom-in at the bottom of CO(3-2) profile. The outflow components are shown as the legends used for CO(2-1). Lower: CO line ratio (r_{32}) , The $\pm 1\sigma$ range of r_{32} is shown in the shadow region.

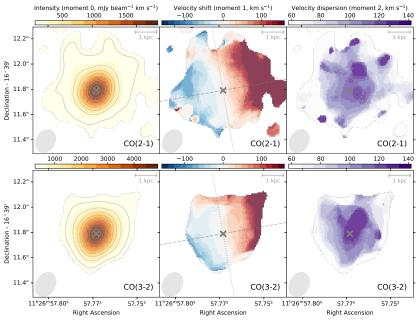


Figure 11. Moment-0, 1, and 2 maps of the beam and MRS-matched cubes of CO(2-1) (top) and CO(3-2) (bottom). Only pixels with intensity S/N > 3 are plotted in each panel. The intensity contours in the left panel start from S/N = 5, with intervals of S/N of 10 for CO(2-1) and 5 for CO(3-2). The dashed and dotted lines in the middle panel represent the major and minor axes of the rotating disk. The grey ellipse shows the beam and the grey cross shows the galaxy center in each panel.

In addition to CO(2-1) and CO(3-2), CO(4-3) line of J1126 is also detected in the unresolved ACA observation. The flux of CO(4-3), 18.5 ± 1.2 Jy km s⁻¹, is extracted in a 2×2 beam-size region as performed for

the 650 μ m continuum. The line ratio of CO(4-3) and CO(2-1) (r_{42}) of the entire galaxy is estimated to be 0.57 using the entire flux of the original CO(2-1) cube within 6 kpc. The ratio is similar to the mean value of local

(U)LIRGs (e.g., 0.5–0.6, Montoya Arroyave et al. 2024). Due to a lack of resolved spatial information for CO(4-3), hereafter we focus on the observation of CO(2-1) and CO(3-2) for kinematic analyses.

4.3. Identification of molecular outflow with CO(2-1) and CO(3-2) observations

4.3.1. Multi-Gaussian fitting of CO lines

Since the CO emission in the sub-millimeter band is less sensitive to dust extinction, both of the redshifted outflow, which is shielded by the dust in the host galaxy in UV/optical observations (e.g., [OIII] 5007Å), and the blueshifted outflow can be observed in the CO line profiles if the outflow is bright. Similar to the identification of ionized outflow, we perform a multi-gaussian fitting for the CO lines, in which a narrow component is used to fit the gas motion in the galaxy disk with one or two broad components for the outflow (hereafter 2-Gaussian and 3-Gaussian fit). The two broad components in the 3-Gaussian fit are adopted to fit the blue- and redshifted outflows separately.

The 3-Gaussian fitting results for CO(2-1) and CO(3-1)2) lines are shown in middle panels in Figure 10. For the CO(2-1) line in the central region (r < 0.5 kpc), both of blue- and redshifted wings are detected in the 3-Gaussian fit, which have a FWHM of 250 km s^{-1} and 450 km s^{-1} , and a flux fraction of 3% and 6%, respectively. The 2-Gaussian best-fit result has a single wing component, which is broader (FWHM = 950 km s^{-1}) and brighter (flux fraction of 14%) than the 3-Gaussian fitting results. However, a half of the wing flux of the 2-Gaussian fitting originates from the low-velocity region (e.g., $|v_{\rm s}| < 200 \,\rm km\,s^{-1}$), which is less significant in kinematics and could be contaminated by the gas motion on the disk. Therefore, we consider that the 3-Gaussian fitting results as a fiducial estimation of the molecular outflow. In the central region (r < 0.5 kpc), the outflow components of CO(3-2) have similar velocities to those of CO(2-1) and a larger flux fractions, 5% and 8%, on the blue- and redshifted sides, respectively. The detailed fitting results are listed in Table C3.

In the galaxy disk scale (r < 3 kpc), the blueshifted outflow becomes faint and makes it difficult to be detected (e.g., with a peak S/N ~ 1 for CO(3-2)). On the other side, both of CO(2-1) and CO(3-2) possess an obvious redshifted wing with the flux fraction even larger than the central region, i.e., 12% for CO(2-1) and 15% for CO(3-2). The different results between the blue-and redshifted outflows suggest an asymmetric outflow structure: the blueshifted outflow is faint and concentrated in the central region, while the redshifted outflow is bright and extended in the galaxy disk scale. Note that even in the center the blueshifted outflow is weaker (e.g., a lower flux fraction) than the redshifted one.

In order to understand the details of the outflow structure, a spatially-resolved analysis is required. However, it is hard to perform the multi-Gaussian fitting for the resolved cubes due to the contamination of the disk motion. Unlike the fast ionized outflow ($|v| > 1000 \, \mathrm{km \, s^{-1}}$), the velocity of molecular outflow is moderate (300–500 $\mathrm{km \, s^{-1}}$) and makes it difficult to separate the outflow from disk motion with the multi-Gaussian fitting in the outskirt region where disk motion shows non-zero velocity shift (e.g., Figure 11, moment-1 map). Another method is required to address the issue.

4.3.2. Decomposition of disk and outflow motions with fitting of the Barolo disk model

In order to determine the spatial distribution of the molecular outflow, in this subsection we adopt the rotating disk model of ^{3D}Barolo(hereafter Barolo; Di Teodoro & Fraternali 2015) to decompose the motion of the molecular gas disk, and then identify the outflow with the non-rotating residuals. In order to reduce the degeneracy of the fitting, we fix the central position of the rotating disk model to the center obtained from the moment-0 map (Figure 11, left); the PA of the model is set to the direction of the major axis estimated with the moment-1 map (Figure 11, middle) with a tolerance of $\pm 5^{\circ}$; the systemic velocity of the disk model is fixed to the value from the narrow component of the 3-Gaussian fitting (e.g., Table C3). We set a primary S/N cut of 5 and a secondary (growing) S/N cut of 3 to determine the fitting region mask. The maps of the best-fit disk model of CO(2-1) and the model-subtracted residuals are shown in Figure 12. The rotating model suggests a disk in a nearly face-on view with an inclination angle of $\sim 20^{\circ}$, which rotates in a counter-clockwise direction along the line of sight and dominates the emission with the observed velocity ($|v_{\rm s}|$) less than 300 km s⁻¹.

The molecular outflow is detected with $|v_s|$ up to 700 km s⁻¹ on both of blue- and redshifted sides in the non-rotating residual maps (Figure 12). The redshifted outflow has a flux-weighted velocity of 350 km s^{-1} . It changes from an unresolved, compact distribution in v_s $> 500 \,\mathrm{km}\,\mathrm{s}^{-1}$, to an extended structure in lower velocity ranges with a radius of 2-3 kpc, which could reflect the deceleration of outflowing gas at a large radius towards the north and west, or the changes of inclination angles of a cone-like outflow structure. The redshifted outflow is brighter than the blueshifted one in all of the velocity bins. The blueshifted outflow shows a flux-weighted velocity of 390 km s⁻¹, similar to that of redshifted outflow. It has a dominant direction to the south in v_s $> 300 \text{ km s}^{-1}$, which is opposite to the redshifted outflow and suggests a bi-conical structure. The orientation of the molecular outflows is consistent with that of the south-tilted (blueshifted) ionized outflow (Section 3.2).

The non-rotating residual maps suggest an asymmetric structure of the molecular outflow: the outflow on the redshifted side is brighter and more extended than that on the blueshifted side. However, there is still uncertainties to determine the extent of the redshifted out-

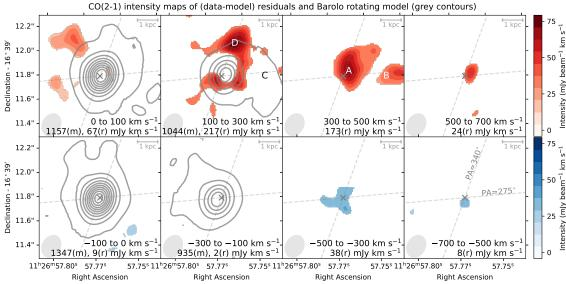


Figure 12. Residual maps of MRS-matched CO(2-1) cube after subtracting the best-fit disk model (contours). The bottom and top panels show the blue- and redshifted sides, respectively. Only pixels with velocity-integrated S/N > 3 are shown. Rotation model is shown in contours starting from model S/N = 3 with an interval of S/N = 10. The fluxes of model (m) and residual (r) integrated with S/N > 3 pixels are shown at bottom in each panel. The grey ellipses denote the beam and the grey cross indicates the galaxy center. The dashed lines show the PA of the PV diagrams shown in Figure 13. See text in Section 4.3.3 for discussion of regions marked with the letter A–D.

flow. For example, an outskirt region of the redshifted outflow shown with the letter "B" in the $300-500~{\rm km\,s^{-1}}$ map of Figure 12 overlaps with a spiral arm-like extension of the rotating disk in lower velocity ranges, i.e., the region "C" in the $100-300~{\rm km\,s^{-1}}$ map. Such overlapping implies a possible non-outflow origination of the extended non-rotating residuals (e.g., "B"), e.g., tidal tails of galaxy merger interaction or an inflowing stream.

4.3.3. Identification of outflow by combination of non-rotating motion and enhanced CO excitation

The relation between molecular outflow and an enhanced CO excitation is shown in the integrated CO lines of J1126 (Figure 10, left-lower panel) and has been reported in local (U)LIRGs (Montoya Arroyave et al. 2024). In order to reduce the possible contamination by other irregular gas motion (e.g., tidal tails) in the spatial identification of the outflow, we combine the method of non-rotating motion with the analysis of spatially resolved CO line ratios using the position-velocity (PV) diagrams.

The PV diagrams are plotted following two lines (i.e., the dashed lines in Figure 12) that passes through the galaxy center with a width of 0.1''. One line with PA of 340° traces the bulk of outflow with 300–500 km s⁻¹ (i.e., the region "A" in Figure 12) and a low-velocity (100–300 km s⁻¹) non-rotating residual region extended to the north (i.e., the region "D"). The line also traces the the main direction of the blueshifted ionized outflow (e.g., Figure 4). The other line with PA of 275° is used to understand the possible association between the pos-

sibly extended outflow in the east, i.e., the region "B" in the 300–500 km s⁻¹ map, and the spiral arm-like extension of the rotating disk, i.e., the region "C" in the 100–300 km s⁻¹ map. The second line is close to the major axis of the molecular gas disk (PA $\sim 280^{\circ}$, see Figure 11).

The PV diagrams of the beam and MRS-matched CO(2-1) and CO(3-2) cubes as well as their line ratio are shown in Figure 13. The best-fit rotating disk models for both of CO(2-1) and CO(3-2) observations are over-plotted as contours in Figure 13. The rotating disk model correlates well with $r_{32} = 1.0$ in the central (r < 0.2''), low-velocity $(|v_s| < 200 \text{ km s}^{-1}) \text{ re-}$ gions. The spiral arm-like extension of the disk, e.g., the region "C", tends to show weaker excitation with $r_{32} \sim 0.6$. On the contrary, the non-rotating components in the central (r < 0.1''), high-velocity $(|v_s| > 300)$ km s⁻¹) regions show stronger excitation with $r_{32} > 1.5$. These intense excitation regions extend to a large radius (0.2"-0.3") as velocity decreases (e.g., due to deceleration as gas travels to the outside) and are mixed with the edges of the rotating disk in the PV diagram.

Although showing a non-rotating motion, the extended regions "B" and "D" mainly correspond to a low r_{32} of 0.5–1.0, which is similar to r_{32} of the spiral arm-like region "C" and lower than that of the central outflow. The low r_{32} indicates that the extended non-rotating residuals can be dominated by non-outflow phenomena (e.g., tidal features).

We combine the method of non-rotating motion and enhanced CO line ratio to identify a "pure" molecular

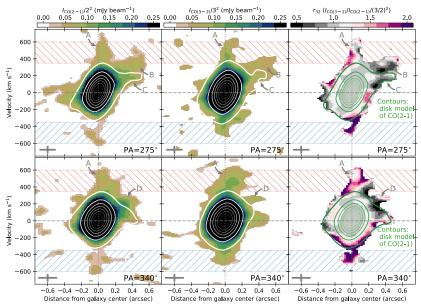


Figure 13. Top: Position-velocity (PV) diagrams of CO(2-1) (left), CO(3-2) (middle), and the line ratios (right). A positive x-axis value shows the direction towards PA = 275° and a negative value towards PA = 95° . In the left and middle panels, the map shows the spectral specific intensity of CO lines averaged within a width of 0.1''. Only spaxels with S/N > 2 are plotted. The contours in the left and middle panels show the best-fit rotating disk models of CO(2-1) and CO(3-2), respectively. The contours in the right panel shows the disk model of CO(2-1). The grey cross in the bottom-left corner represents the spectral (50 km s⁻¹) and spatial resolution (\sim 0.2"). The red and blue hatches denote the velocity ranges of outflow intensity maps in Figure 14. Bottom: The same PV diagrams for PA of 340° (positive x-axis) and 160° (negative x-axis). The legends are the same as those in top panels. The letter A–D correspond to the regions marked in Figure 12. See text in Section 4.3.3 for detailes.

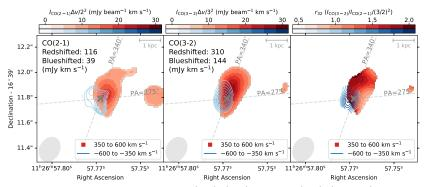


Figure 14. Intensity maps of outflow component of CO(2-1) (left) and CO(3-2) (middle), and the line ratio maps (right). The redshifted outflow is shown in red colored map while the blueshifted one shown in blue contours. The fluxes extracted in pixels with S/N > 3 of CO(2-1) and CO(3-2) are shown in the upper-left corner of each panel. The dashed lines denote the PA of the PV diagrams shown in Figure 13. The beam is shown in grey ellipses and the galaxy center in grey crosses.

outflow by adopting a velocity threshold of 350 km s⁻¹, with which only the non-disk residuals with high r_{32} values are selected. We note that there are several limitations of the treatment. For example, due to the relatively low S/N of CO(3-2) observation, the line ratio cannot traces all of the extended regions in CO(2-1) observation. Furthermore, the relation between a high CO line ratio and the molecular outflow is not fully determined, it is also possible that a high CO excitation only occurs in the outflow close to the galaxy center or the ionizing zone where the gas temperature is high.

The maps of the "pure" outflow component ($|v_{\rm s}| > 350~{\rm km\,s^{-1}}$) of CO(2-1) and CO(3-2) and their line ratio are shown in Figure 14. The upper bound of the velocity range of the maps, $600~{\rm km\,s^{-1}}$, is set based on the central outflow components in the PV diagrams to reduce the data points with a low S/N. On the redshifted side, both of CO(2-1) and CO(3-2) show an extended outflow up to a radius of 1.5 kpc towards PA = 340°. CO (2-1) has an extension up to $r=3~{\rm kpc}$ to the east (PA $\sim 275^{\circ}$), while only a clump is shown in this region of the CO(3-2) map. The blueshifted outflows are fainter and more

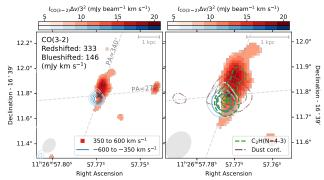


Figure 15. Left: Intensity maps of outflow component of CO(3-2) shown in its original spatial resolution (~ 0.6 kpc). The legends are the same as those of Figure 14. Right: A zoom-in window of the left panel in the center with a width of 3 kpc. The brown dash-dotted and green dashed contours show the distribution of the dust continuum at rest 890 μ m. and the $C_2H(N=4-3)$ line, respectively, with S/N > 3. The green cross denotes the center of C_2H and the grey cross shows the center of CO(3-2) moment-0 map (Figure 11). The frequency integration range of the C_2H contours is shown in Figure 16.

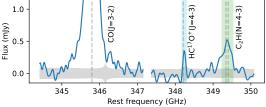


Figure 16. Continuum-subtracted spectrum extracted in the central region (r < 0.25 kpc). The rest frequencies of CO(J=3-2), HC¹⁷O⁺(J=4-3), and C₂H(N=4-3) are shown in vertical dashed lines, in which C₂H has two rest frequencies due to fine structure. The frequency integration ranges of HC¹⁷O⁺(J=4-3) and C₂H(N=4-3) are shown in cyan and green hatched regions, which are used to create the intensity plots shown in Figure 9 and 15. The spectra are convolved by a Gaussian profile with FWHM of 50 km s⁻¹. The 1- σ measurement error is shown in grey regions.

compact than the redshifted ones for both of CO(2-1) and CO(3-2), with a size similar to the beam size.

Finally, we also show the outflow of CO(3-2) in its original spatial resolution, i.e., ~ 0.6 kpc, in Figure 15. The main redshifted outflow in the center is better resolved with a cone-like structure extended to the north following PA = 340° ; while the blueshifted outflow is still not resolved, suggesting a compact distribution. We discuss the possible mechanism behind the asymmetric outflow structure in Section 5.3.

4.4. Association between CO-traced molecular outflow and the ethynyl radical intensity

The spectral setup of the ALMA Cycle 9 observations also covers the rotational transition of the ethynyl radical, $C_2H(N=4-3)$ (hereafter $C_2H(4-3)$), with its spectrum shown in Figure 16. $C_2H(4-3)$ is split into two fine structure lines with rest frequencies of 349.34 (J=9/2-7/2) and 349.40 GHz (J=7/2-5/2), and each of them is split into two hyperfine structure lines⁶, due to the spinorbit and electron-nucleus interactions. Considering the complicated line structure and a moderate S/N of the detection, we do not perform a spatially-resolved fitting as that conducted for CO(3-2). A single-Gaussian fitting for the line profile extracted in a beam-size region in the center (r < 0.3 kpc) results in a FWHM of 200 ${\rm km}\,{\rm s}^{-1}$ with a shift of $-10~{\rm km}\,{\rm s}^{-1}$ from the mean rest frequency of the two fine structure lines. The intensity map of $C_2H(4-3)$ integrated in the velocity range of $\pm 100~{\rm km\,s^{-1}}$ is shown in Figure 15, which shows an alignment to the CO-traced molecular outflow, e.g., a tail extended towards the north (PA = 340°) as the redshifted outflow of CO(3-2). The peak of the $C_2H(4-3)$ intensity is tilted to the south, which is likely correlated with the compact blueshifted outflow of CO(3-2).

The association between the molecular outflow and the ground transition of the ethynyl radical, $C_2H(N=1-0)$, in the nearby Seyfert galaxy NGC 1068 is discussed in García-Burillo et al. (2017) and Saito et al. (2022b). The abundance of C_2H is found to be enhanced in the outflow, which can be produced by the increased number of carbon atoms and ions released by disassociated CO molecules. The CO disassociation is possibly driven by the intense UV and X-ray radiation, and/or the shock-induced icy mantle spluttering as outflow interacts with ISM. These studies support the association between the $C_2H(4-3)$ emission and molecular outflow in J1126.

The $C_2H(4-3)$ transition is reported in several nearby (U)LIRGs, e.g., IRAS 20551-4250 (Imanishi & Nakanishi 2013), NGC 4418 and Arp 220 (Sakamoto et al. 2021). Imanishi & Nakanishi (2013) argued a contribution by the rotational transition of methyl cyanide, $CH_3CN(J=19-18)$ at the frequency. $CH_3CN(J=19-18)$ has a higher dipole moment (i.e., a higher Einstein coefficient thus higher critical density) and a higher excitation temperature (> 200 K vs. 42 K) than $C_2H(4-3)$. The rotationally excited CH₃CN emission is known as a tracer of dense and warm gas in the massive star-forming regions in the Galactic Center region (e.g., Churchwell & Hollis 1983) and starburst galaxies (e.g., Martín et al. 2011). As for the line detected at the frequency in J1126, since its intensity map shows an alignment with the CO(3-2)-traced outflow other than the continuum emitted from the dusty starburst (Figure 15), we consider that C₂H instead of CH₃CN dominants the detection at the frequency.

 $^{^6}$ The hyperfine structure of C₂H(N=4-3) offset by 1 MHz is not resolved in the current observation.

There is another faint emission line in the neighbor of CO(3-2) and C₂H(4-3), i.e., the rotationally excited HC¹⁷O⁺(J=4-3) with a rest frequency of 348.21 GHz⁷. As an isotopomer of HC¹⁶O⁺(J=4-3), HC¹⁷O⁺(J=4-3) traces dense molecular gas (2 × 10⁶ cm⁻³; e.g., Greve et al. 2009). The spectrum and the intensity map integrated with $|v_{\rm s}| < 40~{\rm km\,s^{-1}}$ are shown in Figure 16 and 9, respectively, which is only detected in the galaxy center. Unfortunately, the marginal detection of this line prevents us from performing a detailed analysis of it.

5. DISCUSSIONS

5.1. Comparison of the velocity and spacial extent of the ionized and molecular outflows

The spectra of [OIII] and [OII] as examples of highand low-IP ionized emission lines, as well as CO(2-1)that traces the neutral molecular gas, are shown in Figure 17 (left) for a direct comparison between the multiphase outflows. All of the spectra are extracted from the entire galaxy and normalized at the peak of the entire line profiles. The best-fit profiles instead of the observed data are shown to correct for the instrumental broadening and the contamination of neighboring lines. The original CO(2-1) cube is used to obtain the entire CO(2-1) flux.

The spectra of the ionized and molecular outflows show significant differences in the velocity range and flux fraction of the entire line profile. [OIII] shows an almost fully blueshifted line profile with a maximum velocity $(|v_{10}|)$ of 2400 km s⁻¹. 60% of the [OIII] flux exceeds the escape velocity $(v_{\rm esc})$ of the host galaxy, $\sim 1000 \; {\rm km \, s^{-1}}$, which is estimated following the method in Chen et al. (2020b). [OII] shows a mixed contribution of host disk (i.e., narrow component) and outflow components. The [OII] outflow contributes to 45% of the entire flux and 49% of the [OII] outflow flux exceeds the escape velocity. On the contrary, CO(2-1) shows a much lower outflow fraction, < 10\%, and a significantly lower outflow velocity, $\sim 500 \; \mathrm{km} \, \mathrm{s}^{-1}$, on both of blue- and redshifted sides (for the "pure" molecular outflow discussed in Section 4.3.3). The results reveal that a large fraction of the ionized gas outflow can escape from the gravitational potential of the host galaxy, while the bulk of the molecular gas has not been accelerated by the outflow and even the swept-out molecular gas could not escape from the galaxy (e.g., Toba et al. 2017b).

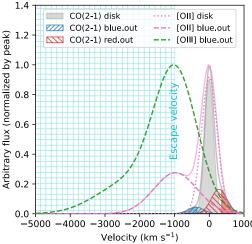
It is also worthy to compare the spatial distributions of the ionized and molecular outflows. Since the PSF of the GMOS observation ($\sim 0.7''$) is much larger than that of the ALMA observation ($\sim 0.2''$ for CO(2-1)), it is hard to directly compare the morphologies of the multi-phase outflows. Similar to the treatment for the spectral profiles discussed above, we perform a Gaussian

fitting to the observed spatial profiles and then correct for the PSF blurring in the best-fit profiles. For the sake of simplicity, the profile fitting and PSF correction are employed in one-dimension following the primary direction of the ionized and molecular outflows, i.e., PA of 160° and 340° . The spatial profile fitting of the CO(2-1) outflow is shown as an example in Figure 18. The observed one-dimensional profiles are obtained from original CO(2-1) cube, which are integrated in [-600, -350] $\mathrm{km}\,\mathrm{s}^{-1}$ and [350, 600] $\mathrm{km}\,\mathrm{s}^{-1}$ on the blue- and redshifted sides, respectively, and averaged in a width of 0.1" following PA of 160° and 340°. The best-fit profiles after correction for the beam blurring ($\sim 1 \text{ kpc}$) (filled regions in Figure 18) are used to represent the intrinsic extent of the molecular outflows on the blue- and redshifted sides. The PSF-corrected profiles of the ionized outflows traced with broad [OIII] and [OII] lines are obtained with the same method and the velocity ranges shown in the left panel of Figure 17. The corrected profiles of the ionized and molecular outflows are shown in the right panel of Figure 17 (normalized at each profile peak). The effective (i.e., half-light) radii of the stellar, ionized gas, and molecular gas disks are also shown for a comparison between the sizes of outflow and disk components. The [OIII] outflow has a shifted center with a distance (d_{cen} ; a negative d_{cen} represents the distance towards the south) of -0.7 kpc and an extent (Δd_{FWHM}) of 3.2 kpc. The [OII] outflow shows a similar distribution with $d_{\rm cen} = -0.5$ kpc and $\Delta d_{\rm FWHM} = 2.8$ kpc. Both of the high- and low-IP ionized outflows show an extended distribution in a galaxy-scale, i.e., comparable to the effective radii of the stellar or ionized gas disks. The blueshifted CO(2-1) outflow shows a compact size $(\Delta d_{\text{FWHM}} = 1.1 \text{ kpc})$ with its center close to the center of the molecular gas disk ($d_{\text{cen}} = -0.1 \text{ kpc}$). Note that although the blueshifted ionized and molecular outflows have different extents, they all show small ratios of $|d_{\rm cen}|/\Delta d_{\rm \scriptscriptstyle FWHM} \sim 0.1$ –0.2, which suggest a nearly faceon view of the outflow cone on the blueshifted side. The different $d_{\rm cen}$ and $\Delta d_{\rm FWHM}$ of the ionized and molecular outflows indicate different positions on the outflow cone, i.e., the molecular outflow locates at the bottom and close to the disk center, while the ionized outflow can travels to a larger distance with a wider distribution.

On the redshifted side only the molecular outflow is detected due to the shielding from the galaxy disk of the UV/optical emissions. The PSF-corrected profile of the redshifted outflow has $d_{\rm cen}=0.5$ kpc and $\Delta d_{\rm FWHM}=1.5$ kpc. A larger ratio, $d_{\rm cen}/\Delta d_{\rm FWHM}=0.3$, of the redshifted outflow is consistent with its elongated morphology towards the north (e.g., Figure 14).

A schematic plot of the spatial structure of the multiphase outflows are shown in Figure 19 in a section along the primary outflow direction. In the scheme the inclination of the galaxy disk is estimated with the Barolo fitting of CO(2-1) cube (Figure 12). An extended ionized outflow and a compact molecular outflow are plotted on

 $^{^7}$ The hyperfine structure of ${\rm HC^{17}O^+(J=4\text{-}3)}$ is not resolved in the current observation.



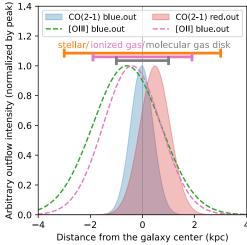


Figure 17. Left: Comparison of the best-fit spectral profiles of ionized gas emission lines, [OIII] and [OII], and molecular gas emission line, CO(2-1). All of the profiles are extracted from the entire galaxy and normalized at the peak of the total line profiles. The profiles of [OIII] (green) and [OII] (purple) have been corrected for the instrumental broadening of GMOS ($\sim 300 \, \mathrm{km \, s^{-1}}$). The disk and outflow components of [OII] are shown in dotted and dashed curves, respectively. The best-fit disk component of CO(2-1) is shown in grey, while the blue- and redshifted outflows are shown in blue and red hatches, respectively. The CO(2-1) outflows with a velocity threshold of $\pm 350 \, \mathrm{km \, s^{-1}}$ are shown as blue and red filled regions to show a "pure" molecular outflow (Section 4.3.3). The cyan hatch denotes the velocity range which exceeds the escape velocity of the host galaxy. Right: Comparison of the one-dimensional spatial profiles of the outflows traced by [OIII] (green dashed), [OII] (purple dashed), and CO(2-1) (blue and red filled regions). A positive value of the x-axis represents the distance from the galaxy center towards the north with PA = 340°. All of the profiles have been corrected for the PSF blurring and normalized at the peak of the outflow intensity profiles. The PSF-corrected effective (i.e., half-light) diameters of the stellar, ionized gas, and molecular gas disks are shown in orange, purple, and grey horizontal lines, respectively, for a comparison with the outflows.

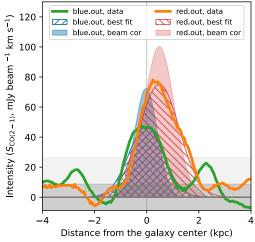


Figure 18. One-dimensional spatial profiles of the CO(2-1) outflows, which are integrated in $[-600, -350] \,\mathrm{km\,s^{-1}}$ and $[350, 600] \,\mathrm{km\,s^{-1}}$ on the blue- and redshifted sides, respectively. The observed data are shown in green and orange for the blue- and redshifted outflows, respectively. The best-fit profiles are marked with hatches and the beam-corrected profiles with filled regions. The $\pm 1\sigma$ and $\pm 3\sigma$ error ranges are shown in dark and light grey, respectively.

the blueshifted side (i.e., near side to the observer). The redshifted molecular outflow could have an orientation close to the disk plane to form a cone-like outflow cavity (e.g., Figure 14). We estimate the dynamical properties of the outflows in Section 5.2 and discuss the possible mechanisms to launch and shape the multi-phase outflows in Section 5.3.

5.2. Estimation and comparison of dynamical quantities of the multi-phase outflows

We start the analyses of the dynamical quantities from the estimation of gas mass in the ionized and molecular outflows. The mass of the ionized outflow is estimated using the broad components of the H α , H β , and the combination of [OII] 3729Å and [OIII] 5007Å lines following the method adopted in Chen et al. (2019) (see also Carniani et al. 2015). The ionized gas mass from the H α emission can be estimated as:

$$\frac{M_{\rm ion}}{10^8 \,\mathrm{M}_{\odot}} = \frac{3.33 L_{\rm H\alpha}}{10^{43} \,\mathrm{erg \ s^{-1}}} \left(\frac{n_{\rm e}}{100 \,\mathrm{cm}^{-3}}\right)^{-1}. \tag{1}$$

A 10% contribution of helium in the ion number density is assumed in the equation. The equation based on ${\rm H}\beta$ can be obtained replacing the factor 3.33 in Equation 1 with 9.52 following the same assumptions. Similarly, we can obtain the estimated ionized gas from the oxygen lines as:

$$\frac{M_{\rm ion}}{10^8 \text{ M}_{\odot}} = \frac{0.88L_{\rm [OII]} + 0.46L_{\rm [OIII]}}{10^{43} \text{ erg s}^{-1}} \left(\frac{n_{\rm e}}{100 \text{ cm}^{-3}}\right)^{-1}.$$
(2)

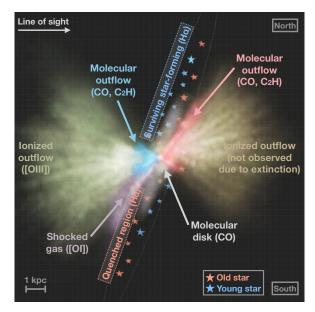


Figure 19. A schematic view of the multi-phase outflows of J1126 in the section along PA of 160° (south) and 340° (north). The inclination of the molecular disk plane (grey) is estimated from the Barolo disk model (Figure 12). The ionized outflow (green fluid) and the shock ionization (violet fluid) regions on the blueshifted side (i.e., near side to the observer) are estimated with the [OIII] intensity map (Figure 4) and the [OI]-traced ionization map (Figure 7), respectively. The molecular outflows on the two sides (blue and red fluids) are estimated with the CO outflow intensity maps (Figure 14). The multi-shell biconical outflow structure is discussed in Section 5.3. A star-forming region survives in the north (near side), which is not significantly affected by the outflow; while the star formation in the southern outflow region (near side) is suppressed (Figure 7 and 21).

In this equation we assume the oxygen ions are mainly in the singly and doubly ionized phases with a solar oxygen abundance in the ionized gas. Solar metallicity is observed as a typical value in local (U)LIRGs (e.g., Pérez-Torres et al. 2021). The dust extinction corrected luminosity of the broad H α , H β , [OII] and [OIII] lines are used to estimate the ionized gas mass, where the extinction, $A_V=1.7$, is estimated using the broad H α /H β ratio (Section 3.4). The electron density of the outflow⁸, $n_{\rm e}=200\pm150~{\rm cm}^{-3}$, is estimated with the ratio of the broad [SII] doublets of the integrated spectrum ($f_{6716}/f_{6731}=1.18\pm0.15$) and the calibration equation of Proxauf et al. (2014). The derived ionized gas mass in the outflow is $1.8\times10^8~M_{\odot}$, $1.8\times10^8~M_{\odot}$, and 1.6×10^8

 M_{\odot} , based on H α , H β , and oxygen lines, respectively. We adopt $M_{\rm ion}=1.8\times 10^8~M_{\odot}$ in later analysis.

The molecular gas mass in the outflow can be estimated with the equation:

$$M_{\rm mol} = \alpha_{\rm CO} \frac{L'_{\rm CO(2-1)}}{r_{21}},$$
 (3)

where $L'_{\text{CO(2-1)}}$ is the luminosity of the outflow component of CO(2-1) in the unit of K km s⁻¹ pc²; r_{21} is the brightness ratio of CO(2-1) over CO(1-0); α_{CO} is the mass conversion factor of CO(1-0) in the unit of M_{\odot} $(K \text{ km s}^{-1} \text{ pc}^2)^{-1}$. In this work we assume the CO(2-1) is thermalized with CO(1-0), i.e., $r_{21} = 1$, which is found as an average value in the nearby (U)LIRGs and AGN host galaxies (e.g., Montoya Arroyave et al. 2023; Molyneux et al. 2024). $\alpha_{CO} = 0.8$ is adopted in the calculation, which is a common assumption in the analyses of (U)LIRGs (e.g., Downes & Solomon 1998; Carilli & Walter 2013; Cicone et al. 2014; Fiore et al. 2017; Veilleux et al. 2020), $M_{\rm mol}$ in the outflow of J1126 is estimated to be $7.4 \times 10^8 \ M_{\odot}$ and $1.7 \times 10^9 \ M_{\odot}$ on the blue- and redshifted sides, respectively, for the "pure" molecular outflow⁹ with $|v_{\rm s}| > 350 \; {\rm km \, s^{-1}}$ (see discussion in Section 4.3.3), which contributes to 4% and 9% of the total molecular gas mass.

The time-averaged mass-loss rate of the outflow can be derived as $\dot{M}_{\rm out} = M_{\rm out}/\Delta t$, where $M_{\rm out}$ is the gas mass in the outflow as estimated above and Δt is the timescale of the outflow, which can be estimated as the ratio of the radius of the outflow over its velocity. For the ionized outflow traced by [OIII] the simplest way to estimate Δt is to use the ratio of the radius and velocity of the bulk of the profile, i.e., $\Delta d_{\sigma}/v_{50} = 1.1$ Myr, where $\Delta d_{\sigma} = \Delta d_{\text{FWHM}}/2.355 = 1.4 \text{ kpc}$ is the PSF-corrected dispersion of the outflow spatial profile (Figure 17, right) and $|v_{50}| = 1210 \text{ km s}^{-1}$ is the 50th percentile velocity of the line spectral profile (Figure 17, left). If we replace Δd_{σ} with the distance of the center of [OIII] outflow, i.e., $|d_{\rm cen}| = 0.7$ kpc, the corresponding Δt is 0.6 Myr. Note that in the above estimation, the inclination of the outflow is not considered, e.g., the velocity is measured along the line of sight while the radii are the values projected on the sky plane. Considering the nearly face-on morphology of the [OIII] outflow, we assume the expansion of the outflow cone in the direction of the sky plane is dominated by the velocity dispersion and the dispersion is isotropic and then, Δt can be estimated as $\Delta d_{\text{FWHM}}/\Delta v_{80} = 1.3 \text{ Myr}$, where $\Delta v_{80} = 2370$ ${\rm km\,s^{-1}}$ is the 80% width of [OIII] spectral profile. The maximum distance and velocity can also be used to derive the timescales of outflows (e.g., Fiore et al. 2017). If we adopt v_{max} as $|v_{10}| = |v_{50}| + \Delta v_{80}/2$ following

⁸ The electron density of the host disk is estimated to be 370 ± 100 cm⁻³ with the ratio of the narrow [SII] doublets, $f_{6716}/f_{6731}=1.05\pm0.07$.

 $^{^9}$ The estimated gas mass in the redshifted molecular outflow can be twice larger if we also consider the low-velocity non-rotating residuals with $v_{\rm s} < 350~{\rm km\,s^{-1}}.$

Chen et al. (2020b) and a similar definition of d_{max} as $|d_{\text{cen}}| + \Delta d_{\text{fWHM}}/2$, the corresponding Δt is 0.9 Myr.

For the molecular outflow traced by CO(2-1), Δt from the $\Delta d_{\sigma}/|\bar{v}_{\rm s}|$ are 1.0 Myr and 1.4 Myr on the blue- and redshifted sides, respectively, where $|\bar{v}_{\rm s}| \sim 450~{\rm km\,s^{-1}}$ is the mean velocity of the "pure" molecular outflow. Δt is estimated to be 0.5 Myr using the center radius of the redshifted outflow (which is not applicable for the blueshifted outflow with a center radius close to zero). Simulation studies indicate the bulk of gas mass of the molecular outflow locates close to the disk plane (e.g., Menci et al. 2019), therefore the expansion with a spherically symmetric dispersion is likely unreasonable for the molecular outflow and we do not estimate Δt with this scenario. Adopting a similar definition of $d_{\rm max}$ and $v_{\rm max}$ as the ionized outflow, Δt is estimated to be 1.0 and 2.0 Myr for the blue- and redshifted outflows, respectively, with the maximum velocities derived from the 3-Gaussian fitting results in the central region $(r < 0.5 \text{ kpc}, \text{ see Table C3}), \text{ i.e., } v_{10} = -660 \text{ km s}^{-1}$ on the blueshifted side and $v_{90} = 620 \text{ km s}^{-1}$ on the redshifted side 10 .

The timescales from the different estimations of the ionized and molecular outflows are approximately consistent with 1 Myr, implying that the multi-phase outflows could be launched in the same period. We adopt $\Delta t=1$ Myr in the later analysis. The corresponding time-averaged mass-loss rate is $180~M_{\odot}~\rm yr^{-1}$ for the blueshifted ionized outflow; $740~M_{\odot}~\rm yr^{-1}$ and $1700~M_{\odot}~\rm yr^{-1}$ for the molecular outflow on the blue- and redshifted sides, respectively. The results can increase by a factor of 3 if we adopt the definition of the instantaneous outflow rate assuming a spherical sector with a uniform density (e.g., Cicone et al. 2014; Fiore et al. 2017).

The momentum rates and the kinetic energy ejection rates (i.e., the kinetic powers) can be derived as $\dot{P}_{\rm out}=\dot{M}_{\rm out}v_{\rm out}$ and $\dot{E}_{\rm k,out}=\dot{M}_{\rm out}v_{\rm out}^2/2$. We adopt $v_{\rm out}$ as the maximum velocity (i.e., $|v_{10}|$ or $|v_{90}|$) which is 2400 km s⁻¹ for the ionized outflow traced with [OIII], 660 km s⁻¹ and 620 km s⁻¹ for the blue- and redshifted molecular outflows traced with CO(2-1), respectively. With the time-averaged $\dot{M}_{\rm out}$, the derived $\dot{P}_{\rm out}$ and $\dot{E}_{\rm k,out}$ of the blueshifted ionized outflow are 2.7×10^{36} dyne and $3.3\times10^{44}~{\rm erg\,s^{-1}}$, respectively. The $\dot{P}_{\rm out}$ and $\dot{E}_{\rm k,out}$ of the molecular outflow are 3.1×10^{36} dyne and $1.0\times10^{44}~{\rm erg\,s^{-1}}$ on the blueshifted side, 6.6×10^{36} dyne and $2.1\times10^{44}~{\rm erg\,s^{-1}}$ on the redshifted side, respectively. These results depend on the choice of $\dot{M}_{\rm out}$ (e.g., an triple increasing using the instantaneous $\dot{M}_{\rm out}$), and the definition of $v_{\rm out}$. Taking the ionized outflow as an example, the derived $\dot{P}_{\rm out}$ changes by a factor of 1.5

with v_{out} defined as $|v_{50}| + 2\Delta v_{\sigma}$ (i.e., $|v_{02}|$ or $|v_{98}|$ for a single Gaussian profile; e.g., Veilleux et al. 2013; Fiore et al. 2017); or by a factor of 0.8 with $v_{\text{out}} = \Delta v_{80}/1.3$ (e.g., Liu et al. 2013). The derived $\dot{E}_{\text{k,out}}$ changes by a factor of 0.7 if we adopt $\dot{E}_{\text{k,out}} = \dot{M}_{\text{out}}(v_{50}^2/2 + 3\Delta v_{\sigma}^2/2)$ assuming a spherically symmetric turbulent motion.

Assuming symmetric ionized outflows on the blueand redshifted sides, the total $\dot{M}_{\rm out}$, $\dot{P}_{\rm out}$, and $\dot{E}_{\rm k,out}$ of the ionized + molecular outflows are 2800 $M_{\odot} \, \mathrm{yr}^{-1}$, 1.5×10^{37} dyne, and 9.6×10^{44} erg s⁻¹, respectively; or 8400 M_{\odot} yr⁻¹, 4.5×10^{37} dyne, and 2.9×10^{45} erg s⁻¹ if the instantaneous $\dot{M}_{\rm out}$ is adopted, e.g., to be compared with the results in the literature (e.g., Cicone et al. 2014; Fiore et al. 2017). The contribution of the neutral atomic gas is not considered in the estimations. Although the absorption lines of neutral sodium at 5896 and 5890Å are covered by the GMOS and SDSS spectra, they are too faint to be detected (e.g., Figure 2). The mass ratio of the outflowing gas in the neutral atomic phase over the ionized phase varies from unity (e.g., Arp 220; Perna et al. 2020) to several tens (Avery et al. 2022) in galaxies in the local universe, therefore the above estimates of J1126 is considered as a lower estimation of the total outflow dynamics.

Figure 20 exhibits the comparison of $\dot{M}_{\rm out}$ and $\dot{E}_{\rm k,out}$ of multi-phase outflows between J1126 and the sample summarized by Fiore et al. (2017). Under the same assumptions adopted by Fiore et al. (2017), e.g., the instantaneous $\dot{M}_{\rm out}$ with outflow velocity defined as v_{02} , J1126 tends to show the highest kinetic values at z < 1 for both of ionized and molecular outflows; the values of the ionized outflow of J1126 is comparable to those of the most luminous AGNs at high-z universe.

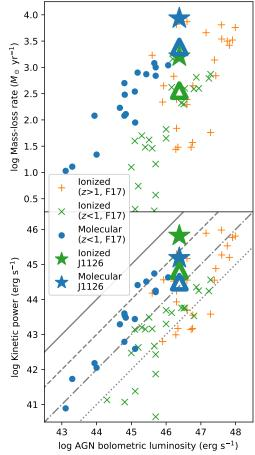
5.3. Mechanisms behind the launching of the multi-phase outflows

The high velocity and the Seyfert-type ionization (Section 3.3) of the ionized outflow suggest that it is driven by a luminous AGN. Since the molecular outflow is aligned with the ionized outflow with a similar primary direction and has a similar outflow timescale, we consider the molecular outflow is also related to AGN activity. Considering the intense star formation activity in J1126, the contribution of starburst to launch the molecular outflow cannot be fully ignored. However, the molecular outflow has different morphologies from that of the central dusty starburst region, i.e., the outflow is elongated while the starburst shows a compact disk-like morphology (Figure 15) and thus, at least the starburst is not the predominant energy source of the outflow.

5.3.1. Galactic outflow driven by an AGN nuclear wind

The so-called "blast-wave" scenario (also called thermal pressure-driven model or wind energy-driven model) is favored to explain powerful galactic outflows in AGN-host galaxies (e.g., Richings & Faucher-Giguère 2018a;

 $^{^{10}}$ Note that the low-velocity range ($|v_{\rm s}|<350~{\rm km\,s^{-1}})$ is included in the Gaussian fitting to derive the maximum velocities, while it is not used in the estimation of the gas mass in the "pure" molecular outflow.



Mass-loss rate (top) and kinetic power (bottom) vs. AGN bolometric luminosity of AGNs in the literature, which are summarized in Fiore et al. (2017) with a uniform set of assumptions. The ionized outflows at z > 1and z < 1 are shown in orange and green crosses; the molecular outflows at z < 1 are shown in blue circles. In order to make a direct comparison between J1126 and the literature studies, the kinetic values of J1126 (stars) are re-calculated following the same method and assumptions used in Fiore et al. (2017), e.g., the instantaneous $\dot{M}_{\rm out}$ with outflow velocity defined as v_{02} . The blue stars denote the kinetic values of the sum of blue- and redshifted molecular outflows of J1126. The green stars denote twice of the kinetic values of the blueshifted ionized outflow under the assumption of symmetric ionized outflows on the blue- and redshifted sides. The blue and green open triangles denote the corresponding values with the method adopted in the paper. The grey lines in the bottom panel mark positions with a loading factor of the kinetic power of 0.1% (dotted), 1% (dashdotted), 10% (dashed), and 100% (solid).

Menci et al. 2019; Costa et al. 2020). In the scenario, a highly ionized, ultrafast (e.g., $> 10^4 \ \rm km \, s^{-1}$) wind is launched in the vicinity of the SMBH, which is thermalized by a reverse shock as it interacts with the ambient medium and expands adiabatically as a hot bubble. The

hot expanding wind sweeps out gas in the host galaxy by its thermal pressure and produce a large-scale outflow. The pre-existing cold molecular gas in the sweptout medium can be disassociated into warm neutral and ionized atomic phases by hydrodynamical instability of a forward shock (e.g., section 2.3.1 in Veilleux et al. 2020, and references therein); while an effective cooling of the swept-out medium can protect the molecular clouds and/or enable the in-situ formation of cold gas in the outflow (e.g., Richings & Faucher-Giguère 2018b; Veilleux et al. 2020). The blast-wave scenario predicts large momentum boosts, e.g., $\dot{P}_{\rm out}/(L_{\rm AGN,bol}/c) \sim 10$ 20 (where $L_{\rm AGN,bol}$ is the AGN bolometric luminosity and c is the speed of light), and high loading factors of kinetic powers, e.g., $\dot{E}_{\rm k,out}/L_{\rm AGN,bol} \sim 1\%-5\%$, with fiducial parameters (e.g. King & Pounds 2015; Richings & Faucher-Giguère 2018a; Costa et al. 2020).

In order to examine whether the energetics of the observed outflow in J1126 matches the prediction of the blast-wave scenario, it is necessary to obtain the estimation of $L_{AGN,bol}$. $L_{AGN,bol}$ can be estimated with the [OIII] luminosity of the AGN-ionized outflow, or the IR luminosity from the dusty torus of AGN. The IRbased method depends on the torus covering factor (e.g., Stalevski et al. 2016; Ichikawa et al. 2019b; Toba et al. 2021). Due to the heavy dust obscuration in the galaxy center (Section 3.4 and 4.1), the torus covering factor could be higher than typical AGNs, which leads to a large uncertainty in the estimated $L_{\rm AGN,bol}$. In addition, the torus emission traces the recent AGN activity, with a light traveling and reprocessed time of ~ 10 years in a 10 pc scale (e.g., Ichikawa & Tazaki 2017), which is too short compared to the outflow timescale of ~ 1 Myr and makes the IR-based $L_{AGN,bol}$ not directly reflecting the launching mechanism of the outflow. Therefore, the extinction corrected 11 $L_{\rm [OIII]}$ is adopted to estimate $L_{\text{AGN,bol}}$. Adopting the empirical relation between the X-ray and [OIII] luminosities (Berney et al. 2015) and the X-ray bolometric corrector (Ricci et al. 2017; Ichikawa et al. 2019b), we obtain $L_{\text{AGN,bol}} = 3.2 \times 10^{46}$ $erg s^{-1}$; a lower estimation, $1.6 \times 10^{46} erg s^{-1}$ is obtained with the X-ray and [OIII] luminosity relation of Ueda et al. (2015). We adopt the mean of the two [OIII]-based $L_{\rm AGN, bol}$, i.e., $2.4 \times 10^{46} {\rm erg \, s^{-1}}$, in the later analysis.

Adopting the time-averaged, total outflow dynamical properties in Section 5.2, the momentum boost and the loading factor of the kinetic power are $\dot{P}_{\rm out}/(L_{\rm AGN,bol}/c)=19$ and $\dot{E}_{\rm k,out}/L_{\rm AGN,bol}=4\%$, which are consistent with the predictions of the blastwave scenario. If we adopt the same assumptions used by Fiore et al. (2017), J1126 will have an extreme load-

¹¹ The shown values in the main text is based on the extinction from the broad component of $H\alpha$ and $H\beta$ lines. If we adopt the extinction from the narrow Balmer lines, the estimated $L_{\rm AGN,bol}$ increases with a factor of 2.6.

ing factor with $\dot{E}_{\rm k,out}/L_{\rm AGN,bol}\sim 20\%$ (Figure 20), which is among the highest values in the literature and is close to the upperlimit value adopted in simulations on galaxy evolution (e.g., Schaye et al. 2015). With the SMBH mass ($M_{\rm SMBH}$) of $6\times10^7~M_{\odot}$, which is estimated from the empirical $M_{\rm SMBH}$ - M_{\star} relation in the local universe (e.g., Reines & Volonteri 2015), the [OIII]-based $L_{\rm AGN,bol}$ corresponds to a super-Eddington accretion, i.e., $\lambda_{\rm Edd}=3.4$, which is efficient to launch a nuclear ultrafast wind (King & Pounds 2015). In addition to the powerful energetics, the blast-wave scenario is also supported by the outflow-induced shock ionization in the galaxy scale (Section 3.3), and the C₂H-traced molecule dissociation in the outflow (Section 4.4).

The multi-phase outflows in J1126 can be explained with the blast-wave scenario accompanying with the galaxy disk (e.g., Menci et al. 2019; Costa et al. 2020), i.e., a massive, low-speed outflow dominated by cold molecular phase locates close to the disk plane, and a less-massive, fast outflow dominated by hot/warm ionized phase travels in the polar direction. The low speed of the molecular outflow is due to the resistance of the galaxy disk with a high ambient density¹², while the dominated molecular phase is the result of the efficient cooling (i.e., due to the low velocity and high density) and the consequent enhancement of the in-situ molecular gas formation (e.g., Richings & Faucher-Giguère 2018b). The fast outflow can persist as it travels through the less dense ambient gas in the polar direction. The strong radiation and fast shock can enhance the ionization and dissociation of molecules; while the high velocity (i.e., high post-shock temperature) and low density reduce the cooling efficiency and suppress the in-situ molecular gas formation. In consequence, a fast, ionized phase dominated outflow is elongated in the polar direction of the disk.

Different from the disk-axisymmetric structure induced by an isotropic nuclear wind in the standard blast-wave model, it is suggested that J1126 possesses inclined outflows, which are tilted to the south and north on the blue- and redshifted sides, respectively, roughly following the opposite orientations (PA $\sim 160^{\circ}$ and 340°; e.g., Figures 4 and 14). Interestingly, the outflows on the two sides could have different inclination angles to the disk plane, which are indicated by the asymmetric line profiles (e.g., Figure 10) and different morphologies (e.g., Figure 14) between the molecular outflows on the two sides. The redshifted outflow could have an inclination closer to the disk plane (as shown in Figure 19), which carves a larger volume of gas out of the disk and create a brighter, more elongated morphology than the

blueshifted outflow. The asymmetric inclinations can also explain the different CO excitation between outflows on the two side (e.g., Figure 10 and 13), i.e., the gas clouds in the blueshifted outflow are more directly exposed in the strong radiation/shock in the galaxy center and are more intensely excited with r_{32} up to 3; while disk shielding on the inclined redshifted outflow could weaken the excitation with a lower r_{32} .

5.3.2. Other possible mechanisms to drive the outflow

The AGN in J1126 could be highly obscured. An almost fully buried AGN with a dust covering factor over 90% is implied by the SKIRTor torus model (Stalevski et al. 2016) based on the IR luminosity of the AGN torus ($2.2 \times 10^{46} \ \mathrm{erg \, s^{-1}}$, estimated from the SED fitting, e.g., Figure 1) and the [OIII]-based $L_{\mathrm{AGN,bol}}$. The highly obscured AGN can also be indicated by the observational evidence that although the ionized outflow exhibits a nearly face-on view, there is no features of Type-1 AGNs (e.g., extremely broad Balmer lines, Balmer continuum, and iron pseudo continua) in the optical spectra. The long spanning between the GMOS and SDSS observations (> 10 years) minimizes the possibility that a compact dusty spot locate along the line of sight incidentally to explain the absence of Type-1 AGN features.

The highly obscured AGN indicates the scenario of the radiation pressure-driven outflow (e.g., Costa et al. 2018), in which the gas is accelerated via the momentum transfer as the optical/UV radiation being absorbed by the dusty medium. Although it is usually considered that the radiation pressure-driving mechanism cannot yield large momentum boosts as that output by the thermal pressure-driven scenario, recent works reported that the model can also provide large momentum boosts when including the trapping of reprocessed IR photons (e.g., Costa et al. 2018; Ishibashi et al. 2021). It is likely that the observed galactic outflow of J1126 is produced with a combination of the thermal pressure-driving by the nuclear hot wind (e.g., high kinetic power and shockinduced ionization/heating) and the radiation pressuredriving by the IR photons (e.g., highly obscured AGN with luminous IR radiation).

The radio jet-driven scenario is considered to be dominated in radio-loud AGNs (e.g., Harrison & Ramos Almeida 2024, and references therein). The radio loudness $(f_{\nu,5{\rm GHz}}/f_{\nu,4400{\rm \AA}})$ of J1126 is 1 or 6 with the extinction-corrected or uncorrected 4400 Å flux and an assumed radio power-law index of 0.8 (e.g., Murphy et al. 2011; Tabatabaei et al. 2017), which categorizes J1126 as a radio-quiet galaxy $(f_{\nu,5{\rm GHz}}/f_{\nu,4400{\rm \AA}} < 10$, e.g., Macfarlane et al. 2021). Therefore, the jet driving is not a dominant mechanism for J1126. After subtracting the star formation-contributed radio luminosity that is estimated with the IR luminosity of ISM dust and the empirical IR-radio relation in star-forming galaxies (e.g., Murphy et al. 2011), the AGN-related radio luminosity is estimated to be $\nu L_{1.4{\rm GHz}} = 1.3 \times 10^{40} \ {\rm erg \, s^{-1}}$,

¹² Since J1126 is observed with a nearly face-on view of the galaxy disk (e.g., Figure 19), the measured velocity of the molecular outflow can be even lower than its intrinsic value due to the projection in the line of sight.

which is 40% of the total radio radiation. The AGN radio luminosity is consistent with the empirical relation between $\nu L_{1.4 \rm GHz}$ and [OIII] velocity (Zakamska & Greene 2014; Hwang et al. 2018), implying that it could originate from the synchrotron emission of electrons accelerated in shocks of the outflow.

Finally, we note that although the star formation driving may not be the dominant mechanism of the outflow (e.g., because of a different morphologies), the stellar wind may enhance the AGN-driven outflow via carrying dust into the ISM, which can either increase the efficiency of the in-situ molecular gas formation in the outflow (e.g., Richings & Faucher-Giguère 2018b) or boost the radiation pressure-driving mechanism (e.g., Ishibashi et al. 2021).

5.4. Feedback effect of the powerful outflow on the host star formation activity

The GMOS and ALMA observations of J1126 reveal a series of effects of the powerful AGN-driven outflow, e.g., the strong ionization by the direct AGN radiation and outflow-induced shocks (Section 3.3), the enhanced excitation of molecular gas (Section 4.3.3), and the large momentum and kinetic power coupled into the multiphase ambient medium in the host galaxy (Section 5.2). In this subsection we discuss the possible instantaneous and long-term effects of the powerful galactic outflow on the stellar mass build-up in the host galaxy of J1126.

5.4.1. A possible instantaneous negative feedback effect

The archived and newly obtained multi-band observations of J1126 provide different SFR estimators, which trace the star formation activity on different timescales and enable us to reconstruct the star formation history (SFH) of J1126. The method for these SFR estimators are described in details in Appendix D. The reproduced SFH is shown in the left panel of Figure 21. The spectral fitting and UV luminosity of the integrated stellar continuum as well as the IR radiation emitted by the ISM dust suggest an averaged SFR of 500–900 $M_{\odot} \,\mathrm{yr}^{-1}$ in the recent 100 Myr. However, the recombination lines of ions (e.g., $H\alpha$) that traces the ionizing photons from the newly formed massive stars, reveal a lower current SFR (timescale of several Myr) of 200 and 50 $M_{\odot} \,\mathrm{yr}^{-1}$ before and after correcting for the contamination of AG-N/shock ionization, respectively. The millimeter freefree emission also suggests a low current SFR with several tens $M_{\odot} \, {\rm yr}^{-1}$. The SFR decay in the recent several Myr implies that J1126 is experiencing a transition from a starburst phase back to the regime of the star formation main sequence (e.g., Peng & Maiolino 2014). Since the transition timescale is close to the outflow traveling time, ~ 1 Myr, a straightforward explanation is that the current star formation activity is suppressed by the outflow as the fueling gas swept-out and/or heated by the powerful outflow, i.e., an instantaneous negative feedback effect.

Another evidence for the negative feedback of outflow is shown by the core-removed intensity map of the narrow $H\alpha$ line (Figure 5), i.e., the $H\alpha$ emission is fainter in the southern outflow region even though the contribution of shock ionized $H\alpha$ emission is larger in the south (Figure 7). In order to reduce the contamination of shock ionization to obtain the the pure star formation ionized $H\alpha$ emission and the corresponding SFR surface density ($\Sigma_{\rm SFR_{H\alpha}}$), we perform a rough approximation with the following equation:

$$\Sigma_{L_{\text{H}\alpha,\text{SF}}} = \frac{\beta_{\text{shock}} \Sigma_{L_{\text{H}\alpha,\text{tot}}} - \Sigma_{L_{[\text{NII}],\text{tot}}}}{\beta_{\text{shock}} - \beta_{\text{SF}}}, \tag{4}$$

where $\Sigma_{L_{\rm H\alpha,tot}}$ and $\Sigma_{L_{\rm [NII],tot}}$ are the extinction corrected, total luminosity surface densities of H α and [NII] lines, while $\Sigma_{L_{
m H}\alpha,
m SF}$ shows the H α emission only from star formation ionizing region; $\beta_{
m SF}$ and $\beta_{
m shock}$ are the ratios, $f_{[NII]}/f_{H\alpha}$, for a pure star formation or shock ionization. In the approximation, we arbitrarily select $\log \beta_{\rm SF} = -0.3$ and $\log \beta_{\rm shock} = 0.1$, which are the boundaries of the composite regime in the BPT diagram (Kewley et al. 2001; Kauffmann et al. 2003) with a mean $\log(f_{\rm [OIII]}/f_{\rm H\beta}) = -0.35$ (see discussion in Section 3.3) and Figure 6). The derived $\Sigma_{L_{\text{H}\alpha,SF}}$ is then converted to $\Sigma_{\rm SFR_{H\alpha}}$ with the calibration of Murphy et al. (2011), which are shown in the middle and right panels of Figure 21 for the original and core-removed GMOS data. In the $\Sigma_{SFR_{H\alpha}}$ map of the original GMOS data, a cavity of low $\Sigma_{\rm SFR_{H\alpha}}$ is shown along the primary direction of the outflow towards the south (PA = 160°). In the cavity, the $H\alpha$ emission is dominated by the shock ionization that is aligned with fast ionized outflow. The $\Sigma_{\rm SFR_{H\alpha}}$ map of the core-removed GMOS data suggests the suppression of $\Sigma_{\rm SFR_{H\alpha}}$ in the south outflow region more apparently¹³. We note that the derived values of $\Sigma_{\rm SFR_{Ho}}$ rely on the arbitrarily selected $\beta_{\rm SF}$ and $\beta_{\rm shock}$, however, a relative suppression of star formation by the outflow can be implied by these results.

The declined current SFR (e.g., from $H\alpha$) compared to the SFR in a longer timescale (e.g., from ISM dust radiation) as well as the suppressed $\Sigma_{\rm SFR_{H\alpha}}$ in the outflow region both suggest an instantaneous negative feedback effect of the powerful outflow. However, the negative feedback may not be the only answer to explain the low SFR (and its surface density) estimated from the faint $H\alpha$ emission, which is also possibly due to the absorption of Lyman continuum photons (Lyc) by dust embedding the newly born massive stars (e.g., Calzetti 2013). The Lyc absorption can directly remove the ionizing pho-

¹³ Due to the shielding of the galaxy disk of UV/optical emissions, the observed Hα map could be dominated by that emitted from the side near to the observer (e.g., Figure 19) and thus, Figure 21 (right panel) indicates a strong feedback towards the south. On the side far from the observer, a profound feedback on star formation in the north is expected, which is indicated by the redshifted CO outflow (e.g., Figure 14).

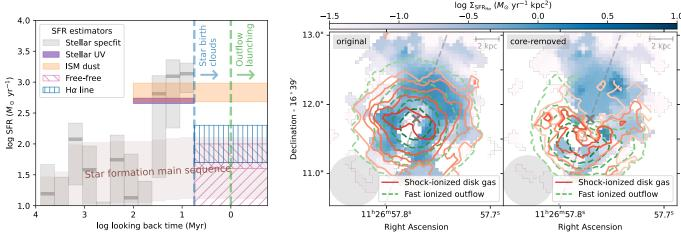


Figure 21. Left: Star formation history (SFH) of J1126 with the SFR estimated from different estimators in different timescales. The grey thick lines represent the best-fit non-parametric SFH from the stellar continuum fitting with the grey filled bars showing the $\pm 1\sigma$ uncertainty in each age bin. The violet bar shows the SFR from the UV flux of the stellar continuum (rest 3500 Å) with the $\pm 1\sigma$ uncertainty from the extinction correction. The orange bar denotes the SFR estimated from the IR luminosity contributed by star formation; its height reflects the uncertainty from the SED fitting and the different calibrations (Murphy et al. 2011; Calzetti 2013). The blue and purple hatches show the SFR estimated from Hα line and free-free emission ("//" for $\alpha_{\rm syn} = 0.8$ and "\\" for $\alpha_{\rm syn} = 1.0$), respectively. The upper bounds of these hatches contain the contamination by AGN activity, while the lower bounds show the contamination-corrected SFR. The blue and green vertical dashed lines show the timescales of the stellar birth clouds and the outflow launching, respectively. The brown shadow region represents the star formation main sequence (Peng & Maiolino 2014) calculated with the accumulated stellar mass in each age bin. See discussion in Appendix D for details of the estimations. Middle: SFR surface density (Σ_{SFRHα}) estimated from the intensity map of narrow Hα line after correction for the shock ionization (see Section 5.4.1 for details of the correction). The intensity of shock-ionized Hα in the disk (i.e., narrow line) is shown in red contours. The fast ionized outflow traced by [OIII] are shown in green dashed contours (see also Figure 5). The grey dashed line denotes the primary outflow direction with PA of 160° and 340° (e.g., Figure 15). PSF are shown in grey circles. Right: The same map as the middle panel for the core-removed GMOS data.

tons emitted by young stars and lead to the faintness of recombination lines (e.g., $H\alpha$) and the thermal freefree emission and thus, an underestimation of SFR from these tracers. The Lyc absorption have been studied for the Galactic massive star-forming regions (MSFRs) (e.g., Inoue et al. 2001; Binder & Povich 2018). Adopting the averaged Lyc absorbed fraction $(f_{C,abs})$ of 50% from the most luminous MSFRs in the sample of Binder & Povich (2018), the H α -based SFR of J1126 could be corrected to 100 $M_{\odot} \, \mathrm{yr}^{-1}$ after removal of the contamination of AGN/shock ionization. Although the Lyc absorption-corrected current SFR is still less than the average SFR in a long timescale, 500–900 $M_{\odot} \text{ yr}^{-1}$, an instantaneous negative feedback is still difficult to be determined because of the large uncertainties to correct for the Lyc absorption and the AGN/shock ionization. An enhanced Lyc absorption (i.e., a larger $f_{C,abs}$) in the central and southern regions of J1126 could also provide a possible non-outflow-quenching explanation for the low measured $\Sigma_{SFR_{H\alpha}}$ in these locations (Figure 21), where the dust extinction tends to be intenser than that in the northern region (e.g., Figure 8).

5.4.2. Implication of long-term feedback effects of the powerful outflow

The intense kinematic effect as well as the strong ionizing/exciting power of the outflow of J1126 indicate the potential to regulate star formation in the host galaxy in a long term. A fraction of 60% of the ionized outflow travels faster than the escape velocity of the host galaxy (Figure 17, left) with a mass-loss rate of 200 M_{\odot} yr⁻¹, assuming the redshifted ionized outflow has the same properties as the observed one on the blueshifted side. Such an amount of gas can be directly removed from the host gas reservoir. Moreover, the ejected-out warm ionized outflow could heat the circumgalactic medium (CGM) with the interaction of them, which can affects cold accretion of CGM onto the galaxy that fuels star formation. A more massive outflow carries molecular gas out of the nuclear star-forming region with a mass-loss rate of 2500 $M_{\odot} \,\mathrm{yr}^{-1}$, which is 3–5 times of the average SFR in the recent starburst duration. Although the molecular outflow cannot escape from the gravitational potential of the host galaxy, the enhanced excitation in the outflow could suggest the heating of gas as it is swept out of the nuclear star-forming region. Consequently, the kinematic removal and/or heating of the powerful

outflow can induce a quenching of star formation in the host galaxy due to starvation of cold fueling gas, i.e., a so-called preventive or delayed feedback (e.g., Veilleux et al. 2020, and references therein).

However, there are also several factors that can limit the feedback effects of the outflow on the host. For instance, the star formation surface density and the ionization maps (e.g., Figure 7 and 21) suggest that only the star formation along the orientation of outflow is profoundly affected, while an active star-forming region can survive in the region away from the main direction of the outflow. Moreover, the kinematic analysis of the molecular gas in the host galaxy reveals an extended spiral arm-like structure with a lower excitation than that of the central disk region (Figure 12 and 13), which probably suggests the inflow of cold fueling gas that locates close to the disk plane and is shielded from the destruction of the outflow.

On the other hand, the powerful galactic outflow also implies the existence of a strong nuclear wind, which is predicted by the blast-wave scenario (Section 5.3.1) and has been found in several ULIRGs/AGNs (e.g., Fiore et al. 2017, and references therein). The nuclear wind may induce the self-feedback on the growth of the central SMBH by clearing out the fueling gas in the vicinity of SMBH, and as a result, reduce the AGN luminosity or even halt the current active accreting period (so-called "fading/dead AGN"; e.g., Ichikawa et al. 2016, 2019a,c; Chen et al. 2020a; Pflugradt et al. 2022). A typical timescale of the high-accretion rate period is 0.01-1 Myr from simulation studies (e.g., Hickox et al. 2014; Ishibashi & Fabian 2022), which is much shorter than the estimated starburst duration of J1126 (~ 30 Myr, Figure 21) and the depletion time by star formation (20– 30 Myr, assumming a constant SFR of the past starburst period). Although it is probably for the central SMBH to experience multiple active accreting periods, these short periods could result in the discontinuous energy output to the outflow and as a consequence, limit the cumulative feedback effect on the host galaxy.

6. SUMMARY

In this paper we report the recent Gemini/GMOS IFU and ALMA observations of a HyLIRG, J1126 at z=0.46842, which is selected from the SDSS-WISE-AKARI cross-matched catalog with an apparent coexistence of a fast ionized outflow and an intense starburst activity. The new observations reveal a powerful, multi-phase outflows with a series of feedback effects on the host galaxy.

• The fast $(v_{10} = 2400 \text{ km s}^{-1})$, [OIII]-traced ionized outflow is found to be extended to several kpc with a $\dot{M}_{\rm out}$ of $180 M_{\odot} \, {\rm yr}^{-1}$ on the blueshifted side. Molecular outflows are detected on both of the blue- and redshifted sides, which have a moderate velocity $(v_{10} = 600 \, {\rm km \, s}^{-1})$ with asymmet-

ric morphologies on the two sides; a high $\dot{M}_{\rm out}$ of 2500 $M_{\odot}\,{\rm yr}^{-1}$ is entrained in the molecular outflow (Section 5.1, and 5.2).

- A large momentum boost and kinetic power suggest the powerful outflow is driven by the blastwave scenario, i.e., the adiabatic expansion of a hot nuclear wind of AGN. The radiation pressure-driving mechanism also probably contributes to the launching of the outflow with a highly obscured AGN (Section 5.3).
- In addition to the high kinetic energy coupled into the ambient ISM, the powerful outflow also affect the host galaxy via inducing a shock ionization (e.g., traced by [OI]; Section 3.3) and enhancing the excitation of the molecular gas (e.g., traced by CO line ratio; Section 4.3.3). Dissociation of molecular gas in the outflow is also suggested with the C₂H observation (Section 4.4).
- A possible instantaneous negative feedback effect is indicated by the declined current SFR compared to the average SFR in a long timescale and the suppressed SFR surface density in the outflow region. However, the low SFR estimated from Hα is also likely due to the absorption of Lyman continuum photons in the dusty birth clouds of young massive stars (Section 5.4.1).
- The high kinetic power and the intense gas ionization/excitation of the outflow suggest the potential to regulate the growth of the host galaxy in a long term via expelling-out and/or heating the cold fueling gas of star formation. However, the cumulative feedback effect could be restricted both in the spatial scale (e.g., a limited volume of the outflow) and the time scale (e.g., a short AGN duty cycle) (Section 5.4.2).

The current GMOS and ALMA observations of J1126 reveal one of the most powerful outflows at the intermediate redshift (Figure 20), multiple feedback mechanisms (e.g., enhanced excitation and dissociation of molecular gas), and the evidence of an in-action negative impact on star formation in the host, which make J1126 a unique laborotary to discover the localized, instantaneous feedback effect of powerful outflows on growth of host galaxies.

There are several remaining puzzles on the nature of the powerful outflow in J1126 and the addressing of them requires future follow-up observations. For example, the kinematics of the ionized gas is unresolved in a stellar bulge scale ($r < 2~\rm kpc$) due to the moderate resolution of ground-based optical observation by Gemini, which prevents a direct comparison of morphologies of the ionized outflow to the molecular outflow observed by ALMA. JWST NIR observation can open a window to

resolve the ionized outflow with a higher resolution (e.g., r < 0.5 kpc). Moreover, currently the enhanced excitation of molecular gas in the outflow is only confirmed with one line ratio (e.g., r_{32}) that leads to degeneracies to determine the gas properties, e.g., temperature and density. ALMA observations of higher-J CO lines can break such degeneracies to reveal more details of the feedback on molecular gas by the outflow. Furthermore, as mentioned in Section 5.4.2 the powerful, galactic outflow could suggest a strong nuclear wind, which may induce a self-feedback on the growth of SMBH and halt the outflow ejection into the host. The feedback in the nuclear region can be investigated with X-ray observations (e.g., NuSTAR) to estimate the current AGN activity, and ALMA observations with super-high resolution (e.g., 100 pc) to determine the properties of the nuclear gas reservoir. We are conducting these multiwavelength follow-ups and will report the results in future papers.

ACKNOWLEDGMENTS

We appreciate the anornymous referee for the constructive suggestions on this paper. X.C. is supported by the ALMA Japan Research Grant of NAOJ ALMA Project, NAOJ-ALMA-349. This work is supported by NAOJ ALMA Scientific Research Grant Code 2023-24A. M.A. is supported by JSPS KAKENHI grant No. JP24K00670. Y.T. is supported by JSPS KAKENHI grant No. JP23K22537. T.K. is supported by Yamada Science Foundation and the Sumitomo Foundation (2200605). D.I. is supported by JSPS KAKENHI

grant No. JP23K20870. M.I. is supported by JSPS KAKENHI grant No. JP21K03632. H.N. aknowledges the support by JSPS KAKENHI No. 19K21884, 20KK0071, 23K20239, 24K00672. The observations were carried out within the framework of Subaru-Gemini time exchange program which is operated by the National Astronomical Observatory of Japan. We are honored and grateful for the opportunity of observing the Universe from Maunakea, which has the cultural, historical and natural significance in Hawaii. This paper makes use of the following ALMA data: ADS/JAO.ALMA #2019.2.00085.S, ADS/JAO.ALMA #2021.1.01496.S, ADS/JAO.ALMA #2022.1.01376.S. ALMA is a partnership of ESO (representing its member states), NSF (USA) and NINS (Japan), together with NRC (Canada), NSTC and ASIAA (Taiwan), and KASI (Republic of Korea), in cooperation with the Republic of Chile. The Joint ALMA Observatory is operated by ESO, AUI/NRAO and NAOJ. Data analysis was carried out on the Multi-wavelength Data Analysis System operated by the Astronomy Data Center (ADC), National Astronomical Observatory of Japan.

Facilities: Gemini-N/GMOS, ALMA, SDSS, Subaru/HSC, 2MASS, WISE, AKARI, VLA

Software: Astropy (Astropy Collaboration et al. 2022), ^{3D}Barolo (Di Teodoro & Fraternali 2015), CASA (McMullin et al. 2007), Gemini IRAF (Gemini Observatory & AURA 2016), L.A.Cosmic (van Dokkum 2001), Matplotlib (Hunter 2007)

APPENDIX

A. METHOD OF SPECTRAL FITTING FOR THE GMOS DATA

We perform the spectral fitting with stellar continuum and emission line components. The stellar continuum is fit with an non-parametric SFH (e.g., Hernandez et al. 2000; Iyer et al. 2019; Ciesla et al. 2023) using the single stellar population (SSP) library of PopStar (Mollá et al. 2009; Millán-Irigoyen et al. 2021). The initial mass function of Kroupa (2001) with stellar masses of 0.1–100 M_{\odot} is adopted. Since there is no nebular continua features (e.g., hydrogen free-bound continuum) of very young stars, we only employ the population with stellar age over 5.5 Myr. A solar metallicity is fixed to reduce the degeneracy in the fitting, which is found as a typical value in local (U)LIRGs (e.g., Pérez-Torres et al. 2021).

The GMOS spectra covers a wide emission line range from [Nev] 3426Å to [SII] 6716,6731Å. Two Gaussian profiles are used to fit each line, with a narrow profile (FWHM $<750~\rm km\,s^{-1})$ for the emission from the disk gas, and a broad profile (750 < FWHM $<2500~\rm km\,s^{-1})$ for the emission from outflowing gas. Since J1126 is

a Type-2 AGN, the Broad-Line-Region of AGN does not contributes to the observed broad line component of permitted line (e.g., $H\alpha$). In order to reduce the degeneracy of fitting, for either narrow or broad components, we tie the kinematic parameters, i.e., velocity shift (v_s) and FWHM, of each emission line (e.g., [OII] and $H\alpha$). An additional broad component (the purple dashed line in bottom panels of Figure 2) with $v_{\rm off} > 2000 {\rm \ km \, s^{-1}}$ is required for [OIII] and H\alpha-[NII] complex, for their blueshifted wing if the peak of the additional component shows S/N > 3. The flux ratios of neighboring lines of the same ion, i.e., [OII] 3726,3729Å, [OIII] 4959,5007Å, and [NII] 6548,6583Å, are fixed to the values calculated with PyNeb (Luridiana et al. 2015) under an electron temperature of 10⁴ K and an electron density of 100 cm^{-3} to reduce the degeneracy of the fitting (Table B2).

The model spectra (stellar continuum plus emission lines) are convolved by the spectral PSF of the GMOS observation ($R \sim 1000$) before fitting to the observed spectra and thus, the output velocity width of both stellar continuum and emission lines reflect the PSF-

corrected value. Monte-Carlo simulations are used to estimate the uncertainty of each fitting parameter. For each observed spectrum, we generate 100 mock spectra via adding random noise normalized by the measurement errors, and perform spectral fitting for the mock spectra. The standard deviations of best-fit parameters of the simulated spectra are used as the uncertainties of best-fit parameters of observed spectra. An example of the spectral fitting for the integrated spectra of J1126 is shown in Figure 2.

The same spectral fitting is performed for both of the original and the core-removed cubes. For either the original or the core-removed cube, we bin adjacent pixels in the faint regions to achieve $\mathrm{S/N} > 5$ for the V-band stellar continuum and $\mathrm{S/N} > 10$ at the peak of the [OIII] line.

A.1. Comparison between the best-fit results of the SDSS and GMOS integrated spectra

We also perform the same spectral fitting for the archived SDSS spectrum of J1126, which is shown as cyan in Figure 2 for a comparison with the results from the GMOS integrated spectrum.

The best-fit fitting of the integrated GMOS spectrum shows the stellar continuum has a velocity shift of $v_{\rm s}=18\pm21~{\rm km\,s^{-1}}$ and FWHM of $777\pm49~{\rm km\,s^{-1}}$. The stellar $v_{\rm s}$ is in relative to the systemic redshift from CO(2-1) ($r<0.5~{\rm kpc}$; Section 4.2) and is consistent with zero considering the uncertainty. The estimated FWHM has been corrected for spectral PSF, and it is consistent with the estimation from SDSS spectrum $688\pm96~{\rm km\,s^{-1}}$ considering the uncertainty. However, there is a relatively large offset between $v_{\rm s}$ from GMOS and SDSS results, which may be due to uncorrected systematic errors between the two instruments since a similar $v_{\rm s}$ offset is also shown in the fitting of narrow emission lines (see Table A1).

Table A1 lists $v_{\rm s}$ and FWHM of the narrow and broad line components in the fitting of the GMOS and SDSS integrated spectra. The narrow components of GMOS and SDSS spectra both show blueshifted velocity in relative to the $v_{\rm s}$ of their stellar continua. As for the estimated FWHM of the narrow components, as well as both of $v_{\rm s}$ and FWHM of the two broad components, the fitting for GMOS and SDSS spectra show consistent results. All of the line widths in Table A1 have been corrected for the instrumental blurring.

B. KINEMATIC PROPERTIES AND INTENSITY MAPS OF THE IONIZED EMISSION LINES

The velocities, fluxes and luminosities of each emission line are listed in Table B2. Figure B1 show the intensity maps of the lines with high ionization potentials (IP). Figure B2, and B3 show the intensity maps of the low-IP lines (and [OI]). The maps of [OIII] and $H\alpha$ are shown in Figure 4 and 5 in the main text.

Table A1. Kinetic measurements of different components.

Component	$v_{\rm s}^{\rm a} ({\rm km s}^{-1})$	$\mathrm{FWHM^b}\ (\mathrm{kms^{-1}})$	
Stellar	$17.8 \pm 21.2^{\rm cd}$	776.5 ± 48.8	
	124.6 ± 33.5	687.7 ± 95.9	
Narrow line	-33.4 ± 2.8	532.0 ± 13.2	
	33.1 ± 13.7	570.6 ± 47.7	
Broad line, 1	-981.3 ± 23.3	1459.8 ± 39.6	
	-920.0 ± 45.5	1622.4 ± 130.2	
Broad line, 2^{e}	-2414.4 ± 155.3	2082.5 ± 215.6	
	-2643.8 ± 266.4	1716.0 ± 634.3	

- ^a The velocity is in relative to the systemic redshift from CO(2-1) (r<0.5 kpc; Tabel C3).
- ^b The width has been corrected for the instrumental broadening.
- ^c The upper value from GMOS integrated spectrum and the bottom value from SDSS spectrum. The same for emission lines.
- ^d Note that all of the uncertainties only reflect those from the measurement noise (via Monte-Carlo simulation), and do not contain systematic errors between different instruments.
- ^e Only used for [OIII] and $H\alpha$ -[NII] complex.

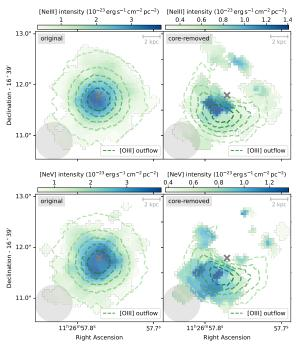


Figure B1. Intensity maps of the outflow components of [NeIII] 3869Å and [NeV] 3426Å from the original (left) and core-removed (right) GMOS data. Both of the two lines show a dominant broad component in its line profile, i.e., as [OIII]. The [OIII] outflow is shown in green dashed contours for a reference. Only pixels with S/N > 3 are shown in the panels.

B.1. Decomposition of broad $H\alpha$ and [NII] lines in the faint outskirt region

The fitting uncertainty of the broad $H\alpha$ and [NII] lines could be large in the outskirt region where S/N is mod-

Line a	v_{50}	Δv_{80}	$f_{ m broad}$	Observed flux	Luminosity b	IP^c
	$(\mathrm{km}\mathrm{s}^{-1})$	$({\rm kms^{-1}})$	(%)	$(10^{-15}\mathrm{erg}\;\mathrm{s}^{-1}\;\mathrm{cm}^{-2})$	$(10^{43} \mathrm{erg \ s^{-1}})$	(eV)
[NeV] 3426 Å	-1096.4 ± 23.4	1654.7 ± 41.3	99.8 ± 0.2	1.61 ± 0.13	1.93 ± 1.76	97.1
$\mathrm{[O{\sc ii}]}\ 3729 \mathrm{\AA}$	-353.1 ± 13.7	1709.3 ± 25.8	44.7 ± 1.9	1.94 ± 0.05	6.08 ± 1.72	13.6
$[\mathrm{Neiii}]~3869\mathrm{\AA}$	-1082.7 ± 23.4	1641.6 ± 42.1	93.7 ± 3.4	1.27 ± 0.08	1.41 ± 0.91	41.0
$_{ m Heta}$	-370.3 ± 22.0	1725.1 ± 24.2	48.6 ± 2.1	1.42 ± 0.04	1.86 ± 0.41	13.6
$\rm [Oiii]5007 \rm \AA$	-1209.6 ± 9.6	2371.2 ± 41.3	96.7 ± 1.0	10.35 ± 0.06	5.89 ± 3.19	35.1
$\mathrm{[OI]6300\AA}$	-92.4 ± 2.8	668.4 ± 10.8	28.5 ± 3.1	0.74 ± 0.04	0.58 ± 0.10	_
$_{ m Hlpha}$	-258.2 ± 17.8	1636.6 ± 65.0	39.0 ± 2.9	8.08 ± 0.50	5.20 ± 1.12	13.6
$[\mathrm{Nii}]~6583\mathrm{\AA}$	-315.9 ± 37.7	2232.1 ± 224.7	43.1 ± 3.7	9.48 ± 0.49	5.73 ± 0.88	14.5
[SII] 6716Å	-256.0 ± 19.0	1627.1 ± 37.8	38.0 ± 2.7	2.06 ± 0.12	1.24 ± 0.21	10.4
[SII] 6731Å	-238.1 ± 24.9	1597.4 ± 50.8	35.4 ± 3.6	1.89 ± 0.07	1.16 ± 0.19	10.4

Table B2. Velocities, fluxes, and luminosities of emission lines from the GMOS integrated spectrum.

^c Ionization potential. The values are adopted from http://astronomy.nmsu.edu/drewski/tableofemissionlines.html. The binding energy of a hydrogen atom, 13.6 eV, is adopted for Balmer lines.

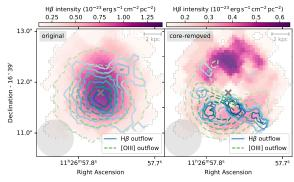


Figure B2. Intensity maps of the narrow components of $H\beta$ from the original (left) and core-removed (right) GMOS data. The $H\beta$ outflow is shown in blue contours. The [OIII] outflow is shown in green dashed contours for a reference. Only pixels with S/N > 3 are shown in the panels.

erate. For an example, the spectra of the central pixel and an outskirt pixel with a distance of 6.5" (4 kpc) are shown in Figure B4 with the fitting uncertainty shown using the mocked spectra. For the bright central spectrum, the broad H α and [NII] lines can be clearly decomposed with S/N of 9 and 7 for the fluxes of the two lines, respectively. However, for the fainter spectrum in the outskirt pixel, the decomposition of broad H α and [NII] lines becomes unstable with the S/N decreasing down to 2 and 3 for the two lines, respectively. The sum of broad H α and [NII] lines is also shown in Figure B4, which can be detected a bit more robustly with the ex-

tended blueshifted wing feature of the $H\alpha$ -[NII] complex and have a higher S/N in the fitting (5 in this case).

We plot the intensity maps of $H\alpha$ and [NII] broad lines and the sum of them in Figure B5. Either of $H\alpha$ or [NII] broad components follows the distribution of [OIII]-traced outflow, e.g., enhanced towards the south in the core-removed map. The $H\alpha+[NII]$ sum intensity shows a closer association with [OIII], which could be a more robust tracer of ionized outflow than the $H\alpha$ - or [NII]-only broad line since the sum has a higher S/N in the fitting.

The $H\alpha$ - and [NII]-only broad lines seems to have different morphologies, e.g., an $H\alpha$ -cavity with a [NII] bright spot following the primary direction of the outflow (PA = 160°) in the south of the core-removed map. The [NII]-bright, $H\alpha$ -faint cavity suggests a strong shock in the outflowing gas, where the broad [OI] and [SII] lines are also enhanced (Figure B3), and could be related to the shock in the host disk gas (i.e., narrow lines) at the same direction (Figure 7 and 21). However, the hardness of the decomposition of broad H α and [NII] lines in outskirt region prevents us from a detailed ionization analysis since all of the line ratios in the BPT diagnostics rely on $H\alpha$. Diagnostics with lines that are not affected by blurring of adjacent lines, e.g., the ratio of [Fe II] $(1.25 \mu m)$ and Pa β (Bianchin et al. 2024), is required to address this question.

^aThe following line doublets are tied with a fixed flux ratio, i.e., $f_{[OII]3726}/f_{[OII]3729} = 0.74$, $f_{[OIII]4959}/f_{[OIII]5007} = 0.34$, and $f_{[NII]6548}/f_{[NII]6583} = 0.34$, for both of their narrow and broad components. These values are calculated with PyNeb under an electron temperature of 10⁴ K and an electron density of 100 cm⁻³.

^b Extinction corrected luminosity. The narrow and broad components are corrected with $A_{V, \text{narrow}} = 3.0$ and $A_{V, \text{broad}} = 1.7$ (Section 3.4), respectively. The shown errors reflect both uncertainties from the measurement error and the extinction correction.

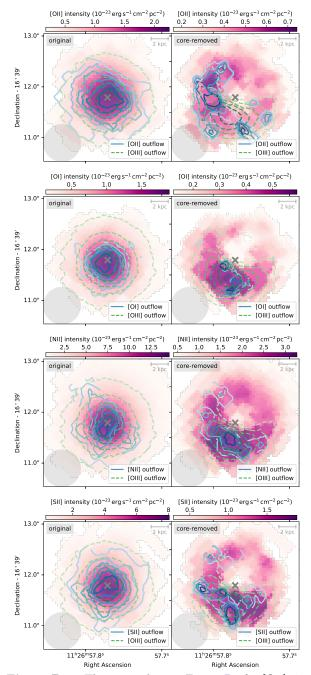


Figure B3. The same plots as Figure B2 for [OII] 3729\AA , [OI] 6300\AA , [NII] 6583\AA , and the sum of [SII] $6716,6731\text{\AA}$ doublets.

C. KINEMATIC PROPERTIES OF MULTI-GAUSSIAN FITTING OF CO LINES

The velocities and the flux fractions of the disk and outflow components of the 3-Gaussian fitting are listed in Table C3. The line profiles of CO(2-1) and CO(3-2) are extracted from the beam and MRS-matched cubes. The line profile of CO(4-3) is extracted from the unresolved ACA data.

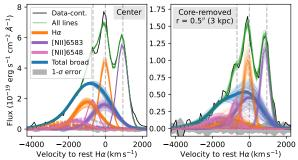


Figure B4. Fitting of the $H\alpha$ -[NII] line complex in the central pixel (left) from the original cube, and an outskirt pixel with a distance of 6.5" from the core-removed cube (shown in an red cross in Figure B5). The continuum-subtracted data is shown in black, while the total line model shown in green. $H\alpha$, [NII] 6583Å, and [NII] 6548Å are shown in orange, violet, and purple, respectively. The narrow components are marked with thin curves that are close to the rest wavelengths (vertical dashed lines) at the systemic redshift. The two broad components of each line are shown in thick solid and dashed curves, respectively. The sum of broad $H\alpha$ and [NII] lines is shown in blue. For all of the fitting components, the thick curve marks the best-fit model of the data while the thin curves denote the results of the mocked spectra to shown the fitting uncertainty. The $\pm 1\sigma$ error range is marked in grey regions.

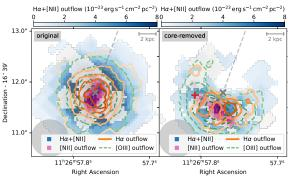


Figure B5. Intensity maps of the sum of broad Hα and [NII] lines (blue) from the original (left) and core-removed (right) GMOS data. The the [NII]only outflow is over-plotted in purple. The Hα-only outflow is shown in orange thick contours while the [OIII]-traced outflow shown in green dashed contours. Only pixels with S/N > 3 are shown for each components. The grey dashed line denotes the primary outflow direction with PA of 160° and 340° . The spectra of pixels locating at the grey (galaxy center) and red crosses are shown in Figure B4.

D. ESTIMATION OF STAR FORMATION HISTORY

The archived and newly obtained multi-band observations of J1126 provide different SFR estimators, which trace the star formation activity on different timescales,

Table C3. Results of 3-Gaussian fitting of CO lines

Component	$v_{ m s}{}^{ m a}$	FWHM	Fraction			
	$(\mathrm{km}\mathrm{s}^{-1})$	$(\mathrm{km}\mathrm{s}^{-1})$	%			
	$CO(2-1) \ (r < 0.5 \ \text{kpc})$					
disk	0.0 ± 0.7	274.4 ± 1.5	91.5 ± 0.7			
blue-wing	-524.1 ± 11.9	253.6 ± 23.9	2.5 ± 0.2			
red-wing	375.0 ± 31.1	449.6 ± 45.1	6.0 ± 0.7			
$CO(2-1) \ (r < 3.0 \ \text{kpc})$						
disk	11.5 ± 1.0	305.7 ± 2.2	85.4 ± 0.9			
blue-wing	-637.5 ± 39.8	401.0 ± 54.6	2.3 ± 0.4			
red-wing	312.1 ± 23.1	596.3 ± 31.3	12.2 ± 0.8			
$CO(3-2) \ (r < 0.5 \ \text{kpc})$						
disk	-0.7 ± 1.1	282.8 ± 2.9	87.7 ± 1.7			
blue-wing	-400.7 ± 19.8	218.3 ± 83.3	4.5 ± 1.0			
red-wing	388.6 ± 25.9	394.1 ± 53.2	7.8 ± 1.1			
$CO(3-2) (r < 3.0 \text{ kpc})^{b}$						
disk	4.9 ± 2.6	296.4 ± 7.0	83.6 ± 3.7			
red-wing	282.1 ± 79.6	641.0 ± 93.4	14.9 ± 3.6			
CO(4-3) (total) ^c						
disk	4.3 ± 5.7	360.5 ± 9.2	_			

- ^a Relative to systemic redshift from CO(2-1) (r < 0.5 kpc).
- ^b The blueshifted wing component is too faint to be detected with a peak $S/N \sim 1$.

and have different model dependencies and limitations, e.g., the contamination of AGN. We try to reconstruct the SFH of J1126 with these SFR estimators. All of them are based on the stellar initial mass function of Kroupa (2001) with stellar masses of 0.1–100 M_{\odot} and a solar metallicity.

We perform the stellar continuum fitting (Appendix A) assuming a non-parametric SFH (e.g., Hernandez et al. 2000; Iyer et al. 2019; Ciesla et al. 2023) utilizing the SSP library of PopStar (Millán-Irigoven et al. 2021) with stellar ages ranging from the age of the Universe at the redshift to the timescale of stellar birth clouds $(t_{\rm BC})$. Stars younger than $t_{\rm BC}$ are highly obscured with a small contribution on the observed stellar light (see discussion in Section 3.4) and thus, they are not considered in the spectral and SFH fitting. Young stars older than $t_{\rm BC}$ and the evolved old stars are assumed to embedded in the diffuse dust with the same extinction amount. We assume $t_{\rm BC} \sim 5.5$ Myr in the fitting. The best-fit SFH is shown as the grey bars in left panel of Figure 21, which consists of an old population with ~ 1 Gyr and a starburst in the recent 5.5–30 Myr with an average SFR of $1700 \pm 500 \ M_{\odot} \, \mathrm{yr}^{-1}$. The average SFR in the recent 5.5–100 Myr is estimated to be 450 ± 140 $M_{\odot} \, \mathrm{yr}^{-1}$. We also estimate SFR using the calibration

with the stellar continuum flux in the UV band (e.g., rest 3500Å) under the assumption of a constant SFR in the recent 100 Myr (Calzetti 2013), which gives $500\pm70~M_{\odot}~\rm yr^{-1}$ with the uncertainty from the extinction correction, i.e, $A_{V,\,\rm stellar}=1.5\pm0.1$ of the diffuse dust (the violet bar in Figure 21, left panel). Since the UV continuum of the newly born stars in the birth clouds is highly obscured, the UV-based SFR is also considered to reflect the formation of stars older than $t_{\rm BC}$, which value is consistent with the averaged SFR in the 5.5–100 Myr by the non-parametric SFH fitting.

The IR radiation reprocessed by the dust heated by the UV and optical light of stars is commonly used to estimate the SFR in recent several tens to 100 Myr (e.g., Calzetti 2013; Murphy et al. 2011). The total IR luminosity (1–1000 μ m) contributed by the star formation heated dust is estimated to be $L_{\rm SF,IR} = (5.5 \pm 1.0) \times 10^{12}$ L_{\odot} from the multi-band SED fitting (Section 4.1), which corresponds to an averaged SFR of 820 and 590 $M_{\odot} \, \mathrm{yr}^{-1}$ with the calibration of Murphy et al. (2011) and Calzetti (2013) for a timescale of 100 Myr, respectively (the orange bar in Figure 21, left panel). The difference between the two estimates is mainly due to the extinction wavelength range of the two calibrations, i.e., Murphy et al. (2011) assumes the Balmer continuum (912– 3646 Å) is absorbed by the dust while Calzetti (2013) assumes the entire stellar bolometric radiation is absorbed. These estimated SFR contains the contribution of both of the stars embedded in the dusty birth clouds and those older than $t_{\rm BC}$, i.e., in the diffuse dust. With the best-fit stellar population and the extinction from the stellar continuum fitting, we can derive the absorbed stellar luminosity, $L_{\rm SF,abs} = 4.4 \times 10^{12} L_{\odot}$. Since the derived $L_{\rm SF,abs}$ only considers the absorbed stellar radiation by the diffuse light, we can the estimate the IR luminosity purely from the dusty birth clouds as, $L_{\rm SF,IR} - L_{\rm SF,abs}$. The corresponding SFR for stars younger than $t_{\rm BC}$ is then estimated to be 150 $M_{\odot}\,{\rm yr}^{-1}$ with the calibration of Calzetti (2013) for a timescale of

Hydrogen recombination lines (e.g., $H\alpha$) and the forbidden metal lines (e.g., [OII] 3726Å) are correlated to the ionizing photons of stars and thus provide estimators of SFR. Since the ionization by stellar light is dominated by massive stars that have a short lifetime, e.g., ~ 5 Myr for O-type stars (Calzetti 2013; Kennicutt et al. 2009), and are highly obscured (see discussion in 3.3), these SFR estimators are considered to sample the current star formation in the dense birth clouds, i.e., $t < t_{\rm BC}$. Utilizing the extinction corrected narrow line components from the GMOS integrated spectrum and the calibrations of Kennicutt et al. (2009), the SFR are estimated to be 220 and 210 M_{\odot} yr⁻¹ with H α and [OII] 3726Å lines, respectively. As discussed in Section 3.3, there is a large contribution of shock ionization for the narrow lines especially in the southern region in the direction the ionized outflow, therefore the SFR esti-

^c Only the disk component is used in the fitting due to a moderate S/N.

mated above should be considered as upper limits. The contamination by the shock ionization can be approximately corrected with the method described in Section 5.4.1 and Equation 4. The pure ${\rm H}\alpha$ -based SFR is then estimated to be 50 $M_{\odot}\,{\rm yr}^{-1}$. The two SFR from the total and shock-corrected ${\rm H}\alpha$ luminosities are shown as upper- and lower bounds of the blue hatch in the left panel of Figure 21.

Finally we estimate the SFR from the free-free emission. The free-free emission in star-forming galaxies originates from the Coulomb interaction between free electrons and ions in thermal equilibrium, which is also correlated to the ionizing photons as the hydrogen recombination lines and provides another current SFR tracer (Calzetti 2013; Murphy et al. 2011). The free-free

luminosity of J1126 can be estimated from the multiband SED fitting (Section 4.1 and Figure 1), which is faint and depends on the assumed index of the synchrotron radio emission ($\alpha_{\rm syn}$). The corresponds SFR is 50 $M_{\odot}\,{\rm yr}^{-1}$ for $\alpha_{\rm syn}=0.8$ and 100 $M_{\odot}\,{\rm yr}^{-1}$ for $\alpha_{\rm syn}=1.0$. Note that there is also a probable contamination by AGN such as the free-free cooling in the AGN-driven galactic outflow. We estimate the contamination by AGN following the theoretical relation between free-free and [OIII] luminosities of Baskin & Laor (2021) and obtain a contamination-corrected SFR of 0 (i.e., the free-free is fully from the cooling of outflow) and 40 $M_{\odot}\,{\rm yr}^{-1}$ for $\alpha_{\rm syn}$ of 0.8 and 1.0, respectively. These results are shown as purple hatches in the left panel of Figure 21.

REFERENCES

- Allen, M. G., Groves, B. A., Dopita, M. A., Sutherland, R. S., & Kewley, L. J. 2008, ApJS, 178, 20, doi: 10.1086/589652
- Arribas, S., Colina, L., Bellocchi, E., Maiolino, R., & Villar-Martín, M. 2014, A&A, 568, A14, doi: 10.1051/0004-6361/201323324
- Astropy Collaboration, Price-Whelan, A. M., Lim, P. L., et al. 2022, ApJ, 935, 167, doi: 10.3847/1538-4357/ac7c74
- Avery, C. R., Wuyts, S., Förster Schreiber, N. M., et al. 2022, MNRAS, 511, 4223, doi: 10.1093/mnras/stac190
- Baldwin, J. A., Phillips, M. M., & Terlevich, R. 1981, PASP, 93, 5, doi: 10.1086/130766
- Barat, D., D'Eugenio, F., Colless, M., et al. 2019, MNRAS, 487, 2924, doi: 10.1093/mnras/stz1439
- Baskin, A., & Laor, A. 2021, MNRAS, 508, 680, doi: 10.1093/mnras/stab2555
- Battisti, A. J., Calzetti, D., & Chary, R. R. 2017, ApJ, 840, 109, doi: 10.3847/1538-4357/aa6fb2
- Benson, A. J., Bower, R. G., Frenk, C. S., et al. 2003, ApJ, 599, 38, doi: 10.1086/379160
- Berney, S., Koss, M., Trakhtenbrot, B., et al. 2015, MNRAS, 454, 3622, doi: 10.1093/mnras/stv2181
- Bianchin, M., U, V., Song, Y., et al. 2024, ApJ, 965, 103, doi: 10.3847/1538-4357/ad2a50
- Binder, B. A., & Povich, M. S. 2018, ApJ, 864, 136, doi: 10.3847/1538-4357/aad7b2
- Bower, R. G., Benson, A. J., Malbon, R., et al. 2006, MNRAS, 370, 645, doi: 10.1111/j.1365-2966.2006.10519.x
- Buton, C., Copin, Y., Aldering, G., et al. 2013, A&A, 549, A8, doi: 10.1051/0004-6361/201219834
- Calzetti, D. 1997, in American Institute of Physics Conference Series, Vol. 408, The ultraviolet universe at low and High redshift, ed. W. H. Waller, 403–412, doi: 10.1063/1.53764

- Calzetti, D. 2013, in Secular Evolution of Galaxies, ed. J. Falcón-Barroso & J. H. Knapen, 419, doi: 10.48550/arXiv.1208.2997
- Calzetti, D., Armus, L., Bohlin, R. C., et al. 2000, ApJ, 533, 682, doi: 10.1086/308692
- Cardelli, J. A., Clayton, G. C., & Mathis, J. S. 1989, ApJ, 345, 245, doi: 10.1086/167900
- Carilli, C. L., & Walter, F. 2013, ARA&A, 51, 105, doi: 10.1146/annurev-astro-082812-140953
- Carniani, S., Marconi, A., Maiolino, R., et al. 2015, A&A, 580, A102, doi: 10.1051/0004-6361/201526557
- Charlot, S., & Fall, S. M. 2000, ApJ, 539, 718, doi: 10.1086/309250
- Chen, X., Akiyama, M., Noda, H., et al. 2019, PASJ, 71, 29, doi: 10.1093/pasj/psz002
- Chen, X., Ichikawa, K., Noda, H., et al. 2020a, ApJL, 905, L2, doi: 10.3847/2041-8213/abca30
- Chen, X., Akiyama, M., Ichikawa, K., et al. 2020b, ApJ, 900, 51, doi: 10.3847/1538-4357/aba599
- Churchwell, E., & Hollis, J. M. 1983, ApJ, 272, 591, doi: 10.1086/161322
- Cicone, C., Maiolino, R., Sturm, E., et al. 2014, A&A, 562, A21, doi: 10.1051/0004-6361/201322464
- Cicone, C., Severgnini, P., Papadopoulos, P. P., et al. 2018, ApJ, 863, 143, doi: 10.3847/1538-4357/aad32a
- Ciesla, L., Gómez-Guijarro, C., Buat, V., et al. 2023, A&A, 672, A191, doi: 10.1051/0004-6361/202245376
- Ciotti, L., & Ostriker, J. P. 1997, ApJL, 487, L105, doi: 10.1086/310902
- Costa, T., Pakmor, R., & Springel, V. 2020, MNRAS, 497, 5229, doi: 10.1093/mnras/staa2321
- Costa, T., Rosdahl, J., Sijacki, D., & Haehnelt, M. G. 2018, MNRAS, 479, 2079, doi: 10.1093/mnras/sty1514

- Cresci, G., Marconi, A., Zibetti, S., et al. 2015, A&A, 582, A63, doi: 10.1051/0004-6361/201526581
- Di Teodoro, E. M., & Fraternali, F. 2015, MNRAS, 451, 3021, doi: 10.1093/mnras/stv1213
- Downes, D., & Solomon, P. M. 1998, ApJ, 507, 615, doi: 10.1086/306339
- Ellison, S. L., Wong, T., Sánchez, S. F., et al. 2021, MNRAS, 505, L46, doi: 10.1093/mnrasl/slab047
- Fabian, A. C. 2012, ARA&A, 50, 455, doi: 10.1146/annurev-astro-081811-125521
- Falstad, N., Aalto, S., König, S., et al. 2021, A&A, 649, A105, doi: 10.1051/0004-6361/202039291
- Ferland, G. J., & Netzer, H. 1983, ApJ, 264, 105, doi: 10.1086/160577
- Ferrarese, L., & Merritt, D. 2000, ApJL, 539, L9, doi: 10.1086/312838
- Fiore, F., Feruglio, C., Shankar, F., et al. 2017, A&A, 601, A143, doi: 10.1051/0004-6361/201629478
- Fried, D. L. 1965, Journal of the Optical Society of America (1917-1983), 55, 1427, doi: 10.1364/JOSA.55.001427
- García-Bernete, I., Rigopoulou, D., Aalto, S., et al. 2022, A&A, 663, A46, doi: 10.1051/0004-6361/202142749
- García-Burillo, S., Viti, S., Combes, F., et al. 2017, A&A, 608, A56, doi: 10.1051/0004-6361/201731862
- Geach, J. E., Hickox, R. C., Diamond-Stanic, A. M., et al. 2014, Nature, 516, 68, doi: 10.1038/nature14012
- Gebhardt, K., Bender, R., Bower, G., et al. 2000, ApJL, 539, L13, doi: 10.1086/312840
- Gemini Observatory, & AURA. 2016, Gemini IRAF: Data reduction software for the Gemini telescopes, Astrophysics Source Code Library, record ascl:1608.006
- Genzel, R., Förster Schreiber, N. M., Rosario, D., et al. 2014, ApJ, 796, 7, doi: 10.1088/0004-637X/796/1/7
- Greve, T. R., Papadopoulos, P. P., Gao, Y., & Radford,
 S. J. E. 2009, ApJ, 692, 1432,
 doi: 10.1088/0004-637X/692/2/1432
- Harrison, C. M., Alexander, D. M., Mullaney, J. R., & Swinbank, A. M. 2014, MNRAS, 441, 3306, doi: 10.1093/mnras/stu515
- Harrison, C. M., & Ramos Almeida, C. 2024, Galaxies, 12, 17, doi: 10.3390/galaxies12020017
- Harrison, C. M., Alexander, D. M., Swinbank, A. M., et al. 2012, MNRAS, 426, 1073, doi: 10.1111/j.1365-2966.2012.21723.x
- Hernandez, X., Gilmore, G., & Valls-Gabaud, D. 2000, MNRAS, 317, 831, doi: 10.1046/j.1365-8711.2000.03809.x
- Hickox, R. C., Mullaney, J. R., Alexander, D. M., et al. 2014, ApJ, 782, 9, doi: 10.1088/0004-637X/782/1/9
- Hinkle, J. T., Veilleux, S., & Rupke, D. S. N. 2019, ApJ, 881, 31, doi: 10.3847/1538-4357/ab2bfa

- Hinshaw, G., Larson, D., Komatsu, E., et al. 2013, ApJS, 208, 19, doi: 10.1088/0067-0049/208/2/19
- Hopkins, P. F., Hernquist, L., Cox, T. J., & Kereš, D. 2008, ApJS, 175, 356, doi: 10.1086/524362
- Hunter, J. D. 2007, Computing in Science & Engineering, 9, 90, doi: 10.1109/MCSE.2007.55
- Hwang, H.-C., Zakamska, N. L., Alexandroff, R. M., et al. 2018, MNRAS, 477, 830, doi: 10.1093/mnras/sty742
- Ichikawa, K., & Tazaki, R. 2017, ApJ, 844, 21, doi: 10.3847/1538-4357/aa7891
- Ichikawa, K., Ueda, J., Bae, H.-J., et al. 2019a, ApJ, 870, 65, doi: 10.3847/1538-4357/aaf233
- Ichikawa, K., Ueda, J., Shidatsu, M., Kawamuro, T., & Matsuoka, K. 2016, PASJ, 68, 9, doi: 10.1093/pasj/psv112
- Ichikawa, K., Ricci, C., Ueda, Y., et al. 2019b, ApJ, 870, 31, doi: 10.3847/1538-4357/aaef8f
- Ichikawa, K., Kawamuro, T., Shidatsu, M., et al. 2019c, ApJL, 883, L13, doi: 10.3847/2041-8213/ab3ebf
- Imanishi, M., & Nakanishi, K. 2013, AJ, 146, 91, doi: 10.1088/0004-6256/146/4/91
- Inoue, A. K., Hirashita, H., & Kamaya, H. 2001, ApJ, 555, 613, doi: 10.1086/321499
- Ishibashi, W., & Fabian, A. C. 2022, MNRAS, 516, 4963, doi: 10.1093/mnras/stac2614
- Ishibashi, W., Fabian, A. C., & Arakawa, N. 2021, MNRAS, 502, 3638, doi: 10.1093/mnras/stab266
- Iyer, K. G., Gawiser, E., Faber, S. M., et al. 2019, ApJ, 879, 116, doi: 10.3847/1538-4357/ab2052
- Jones, A. P., Köhler, M., Ysard, N., Bocchio, M., & Verstraete, L. 2017, A&A, 602, A46, doi: 10.1051/0004-6361/201630225
- Kauffmann, G., Heckman, T. M., Tremonti, C., et al. 2003, MNRAS, 346, 1055, doi: 10.1111/j.1365-2966.2003.07154.x
- Kennicutt, Robert C., J., Hao, C.-N., Calzetti, D., et al. 2009, ApJ, 703, 1672,
 - doi: 10.1088/0004-637X/703/2/1672
- Kewley, L. J., Dopita, M. A., Leitherer, C., et al. 2013, ApJ, 774, 100, doi: 10.1088/0004-637X/774/2/100
- Kewley, L. J., Dopita, M. A., Sutherland, R. S., Heisler,C. A., & Trevena, J. 2001, ApJ, 556, 121,doi: 10.1086/321545
- Kewley, L. J., Groves, B., Kauffmann, G., & Heckman, T. 2006, MNRAS, 372, 961, doi: 10.1111/j.1365-2966.2006.10859.x
- Khandai, N., Di Matteo, T., Croft, R., et al. 2015, MNRAS, 450, 1349, doi: 10.1093/mnras/stv627
- King, A. 2005, ApJL, 635, L121, doi: 10.1086/499430

- King, A., & Pounds, K. 2015, ARA&A, 53, 115, doi: 10.1146/annurev-astro-082214-122316
- Kirkpatrick, A., Sharon, C., Keller, E., & Pope, A. 2019, ApJ, 879, 41, doi: 10.3847/1538-4357/ab223a
- Kopsacheili, M., Zezas, A., & Leonidaki, I. 2020, MNRAS, 491, 889, doi: 10.1093/mnras/stz2594
- Kormendy, J., & Ho, L. C. 2013, ARA&A, 51, 511, doi: 10.1146/annurev-astro-082708-101811
- Koyama, Y., Shimakawa, R., Yamamura, I., Kodama, T., & Hayashi, M. 2019, PASJ, 71, 8, doi: 10.1093/pasj/psy113Kroupa, P. 2001, MNRAS, 322, 231,
- doi: 10.1046/j.1365-8711.2001.04022.x
- Lammers, C., Iyer, K. G., Ibarra-Medel, H., et al. 2023, ApJ, 953, 26, doi: 10.3847/1538-4357/acdd57
- Li, N., Li, C., Mo, H., et al. 2021, ApJ, 917, 72, doi: 10.3847/1538-4357/ac0973
- Lin, Z., & Kong, X. 2020, ApJ, 888, 88, doi: 10.3847/1538-4357/ab5f0e
- Liu, G., Zakamska, N. L., Greene, J. E., Nesvadba, N. P. H., & Liu, X. 2013, MNRAS, 436, 2576, doi: 10.1093/mnras/stt1755
- Luridiana, V., Morisset, C., & Shaw, R. A. 2015, A&A, 573, A42, doi: 10.1051/0004-6361/201323152
- Macfarlane, C., Best, P. N., Sabater, J., et al. 2021, MNRAS, 506, 5888, doi: 10.1093/mnras/stab1998
- Maiolino, R., Russell, H. R., Fabian, A. C., et al. 2017, Nature, 544, 202, doi: 10.1038/nature21677
- Martín, S., Krips, M., Martín-Pintado, J., et al. 2011, A&A, 527, A36, doi: 10.1051/0004-6361/201015855
- McMullin, J. P., Waters, B., Schiebel, D., Young, W., & Golap, K. 2007, in Astronomical Society of the Pacific Conference Series, Vol. 376, Astronomical Data Analysis Software and Systems XVI, ed. R. A. Shaw, F. Hill, & D. J. Bell, 127
- Menci, N., Fiore, F., Feruglio, C., et al. 2019, ApJ, 877, 74, doi: 10.3847/1538-4357/ab1a3a
- Millán-Irigoyen, I., Mollá, M., Cerviño, M., et al. 2021, MNRAS, 506, 4781, doi: 10.1093/mnras/stab1969
- Mollá, M., García-Vargas, M. L., & Bressan, A. 2009, MNRAS, 398, 451, doi: 10.1111/j.1365-2966.2009.15160.x
- Molyneux, S. J., Calistro Rivera, G., De Breuck, C., et al. 2024, MNRAS, 527, 4420, doi: 10.1093/mnras/stad3133
- Montoya Arroyave, I., Cicone, C., Makroleivaditi, E., et al. 2023, A&A, 673, A13, doi: 10.1051/0004-6361/202245046
- Montoya Arroyave, I., Cicone, C., Andreani, P., et al. 2024, arXiv e-prints, arXiv:2402.17851, doi: 10.48550/arXiv.2402.17851
- Murphy, E. J., Condon, J. J., Schinnerer, E., et al. 2011, ApJ, 737, 67, doi: 10.1088/0004-637X/737/2/67

- Nelson, D., Pillepich, A., Springel, V., et al. 2018, MNRAS, 475, 624, doi: 10.1093/mnras/stx3040
- Peng, Y.-j., & Maiolino, R. 2014, MNRAS, 443, 3643, doi: 10.1093/mnras/stu1288
- Pérez-Torres, M., Mattila, S., Alonso-Herrero, A., Aalto, S., & Efstathiou, A. 2021, A&A Rv, 29, 2, doi: 10.1007/s00159-020-00128-x
- Perna, M., Arribas, S., Catalán-Torrecilla, C., et al. 2020, A&A, 643, A139, doi: 10.1051/0004-6361/202038328
- Perrotta, S., Hamann, F., Zakamska, N. L., et al. 2019, MNRAS, 488, 4126, doi: 10.1093/mnras/stz1993
- Peterson, J. R., Kahn, S. M., Paerels, F. B. S., et al. 2003, ApJ, 590, 207, doi: 10.1086/374830
- Pflugradt, J., Ichikawa, K., Akiyama, M., et al. 2022, ApJ, 938, 75, doi: 10.3847/1538-4357/ac8ff3
- Privon, G. C., Aalto, S., Falstad, N., et al. 2017, ApJ, 835, 213, doi: 10.3847/1538-4357/835/2/213
- Proxauf, B., Öttl, S., & Kimeswenger, S. 2014, A&A, 561, A10, doi: 10.1051/0004-6361/201322581
- Reines, A. E., & Volonteri, M. 2015, ApJ, 813, 82, doi: 10.1088/0004-637X/813/2/82
- Ricci, C., Trakhtenbrot, B., Koss, M. J., et al. 2017, ApJS, 233, 17, doi: 10.3847/1538-4365/aa96ad
- Rich, J. A., Dopita, M. A., Kewley, L. J., & Rupke, D. S. N. 2010, ApJ, 721, 505, doi: 10.1088/0004-637X/721/1/505
- Richings, A. J., & Faucher-Giguère, C.-A. 2018a, MNRAS, 478, 3100, doi: 10.1093/mnras/sty1285
- 2018b, MNRAS, 474, 3673, doi: 10.1093/mnras/stx3014
 Roddier, F. 1981, Progess in Optics, 19, 281, doi: 10.1016/S0079-6638(08)70204-X
- Rupke, D. S. N., Coil, A., Geach, J. E., et al. 2019, Nature, 574, 643, doi: 10.1038/s41586-019-1686-1
- Saito, T., Takano, S., Harada, N., et al. 2022a, ApJL, 927, L32, doi: 10.3847/2041-8213/ac59ae
- —. 2022b, ApJ, 935, 155, doi: 10.3847/1538-4357/ac80ff
- Sakamoto, K., González-Alfonso, E., Martín, S., et al. 2021, ApJ, 923, 206, doi: 10.3847/1538-4357/ac2746
- Santoro, F., Rose, M., Morganti, R., et al. 2018, A&A, 617, A139, doi: 10.1051/0004-6361/201833248
- Schaye, J., Crain, R. A., Bower, R. G., et al. 2015, MNRAS, 446, 521, doi: 10.1093/mnras/stu2058
- Schlafly, E. F., & Finkbeiner, D. P. 2011, ApJ, 737, 103, doi: 10.1088/0004-637X/737/2/103
- Shin, J., Woo, J.-H., Chung, A., et al. 2019, ApJ, 881, 147, doi: 10.3847/1538-4357/ab2e72
- Stalevski, M., Ricci, C., Ueda, Y., et al. 2016, MNRAS, 458, 2288, doi: 10.1093/mnras/stw444
- Storey, P. J., & Hummer, D. G. 1995, MNRAS, 272, 41, doi: 10.1093/mnras/272.1.41

- Sturm, E., González-Alfonso, E., Veilleux, S., et al. 2011, ApJL, 733, L16, doi: 10.1088/2041-8205/733/1/L16
- Tabatabaei, F. S., Schinnerer, E., Krause, M., et al. 2017, ApJ, 836, 185, doi: 10.3847/1538-4357/836/2/185
- Toba, Y., Bae, H.-J., Nagao, T., et al. 2017a, ApJ, 850, 140, doi: 10.3847/1538-4357/aa918a
- Toba, Y., Komugi, S., Nagao, T., et al. 2017b, ApJ, 851, 98, doi: 10.3847/1538-4357/aa9d17
- Toba, Y., Ueda, Y., Gandhi, P., et al. 2021, ApJ, 912, 91, doi: 10.3847/1538-4357/abe94a
- Toba, Y., Yamada, S., Matsubayashi, K., et al. 2022, PASJ, 74, 1356, doi: 10.1093/pasj/psac073
- Tombesi, F., Meléndez, M., Veilleux, S., et al. 2015, Nature, 519, 436, doi: 10.1038/nature14261
- Ueda, Y., Hashimoto, Y., Ichikawa, K., et al. 2015, ApJ, 815, 1, doi: 10.1088/0004-637X/815/1/1

- van Dokkum, P. G. 2001, PASP, 113, 1420, doi: 10.1086/323894
- Veilleux, S., Kim, D. C., Sanders, D. B., Mazzarella, J. M., & Soifer, B. T. 1995, ApJS, 98, 171, doi: 10.1086/192158
- Veilleux, S., Maiolino, R., Bolatto, A. D., & Aalto, S. 2020, A&A Rv, 28, 2, doi: 10.1007/s00159-019-0121-9
- Veilleux, S., Meléndez, M., Sturm, E., et al. 2013, ApJ, 776, 27, doi: 10.1088/0004-637X/776/1/27
- Woo, J.-H., Son, D., & Bae, H.-J. 2017, ApJ, 839, 120, doi: 10.3847/1538-4357/aa6894
- Zakamska, N. L., & Greene, J. E. 2014, MNRAS, 442, 784, doi: 10.1093/mnras/stu842
- Zakamska, N. L., Hamann, F., Pâris, I., et al. 2016, MNRAS, 459, 3144, doi: 10.1093/mnras/stw718